Article:
Chen, W., Shi, C., Ding, J. et al. (2 more authors) (2025) Data-driven sparse learning of three-dimensional subsurface properties incorporating random field theory. Engineering Geology, 349. 107972. ISSN 0013-7952

https://doi.org/10.1016/j.enggeo.2025.107972

Data-Driven Sparse Learning of Three-dimensional Subsurface Properties Incorporating Random Field Theory

Weihang Chen [a], **Chao Shi** [b], **Jianwen Ding** [a,*], **Tengfei Wang** [c,d], **David P. Connolly** [e]

[a] School of Transportation, Southeast University, Nanjing 210096, China

[b] School of Civil and Environmental Engineering, Nanyang Technological University, Singapore 639798, Singapore

[c] School of Civil Engineering, Southwest Jiaotong University, Chengdu 610031, China

[d] MOE Key Laboratory of High-Speed Railway Engineering, Southwest Jiaotong University, Chengdu 610031, China

[e] School of Civil Engineering, University of Leeds, Leeds LS2 9JT, UK

* Corresponding author

Email: jwding@seu.edu.cn

Abstract

Geotechnical engineers rely on accurate soil property information for engineering analyses. However, it is challenging for spatial learning of soil attributes because in-situ geotechnical testing is typically performed sparsely at discrete locations, and soil properties also exhibit inherent spatial variability. Traditional geostatistical methods for predicting spatial properties at these unsampled locations exhibit high computational complexity and require pre-determination of hyper-parameters, while pure data-driven methods fail to integrate geotechnical knowledge. In this study, a hybrid and parameter-free framework that uses random field theory and machine learning is proposed to model 3D subsurface field with reduced computational complexity. The framework constructs site-specific basis functions for characterizing the spatial variations of soil properties by decomposing a correlation matrix through principal component analysis. To further reduce the computational complexity involved in processing high-dimensional correlation matrices, a sparse sampling strategy is adopted to map correlation matrix onto lower-rank principal component space. A series of synthetic random field examples are generated to illustrate the impact of scale of fluctuation and autocorrelation functions on the accuracy and sensitivity of subsurface modeling. The performance of the proposed method is further validated using both synthetic cases and two real case histories. It is demonstrated that the proposed method generally achieves higher R^2 and lower root mean square error (RMSE) and mean absolute percentage error (MAPE) compared to state-of-the-art methods, such as Kriging and Bayesian compressive sensing. Moreover, the proposed method facilitates the explicit quantification of uncertainty associated with the subsurface models, providing valuable insights for engineering design and analysis. The data and code used in this study are available at https://github.com/Data-Driven-RFT/Sparse-Learning.

Keywords: Geotechnical spatial variability; Machine learning aided geotechnics; Random field theory; Geotechnical site investigation; Principal component analysis

1 Introduction

The earth's historical geological and environmental processes have resulted in significant spatial variability in near-surface soil deposits and thus geotechnical engineering properties (Gong et al., 2021; Phoon et al., 2022; Shi and Wang, 2023). It is widely accepted in engineering geology and geotechnical engineering that this spatial variability affects the interaction between geotechnical structures and the soil, serving as a major source of engineering uncertainty (Jiang et al., 2024b; Liu et al., 2023; Wang and Shi, 2023; Zhang et al., 2020). Accurate subsurface models which characterize the spatial distribution of soil properties, can aid engineers in conducting more rational analyses and optimized designs (Chen et al., 2023; Qiu et al., 2024; Wang et al., 2020; Zhao et al., 2020). Despite its importance, time constraints, financial considerations, and site-specific limitations often restrict investigation to sparsely located spot-testing. For example, cone penetration test (CPT) is widely used for its simplicity and cost-effectiveness, but CPT tests are typically conducted at intervals of tens of meters along the surface, providing only sparse information about the complex spatial distribution of soil properties (Collico et al., 2024; Guan et al., 2020; Xie et al., 2022b). Consequently, constructing accurate and reliable subsurface models using such sparse investigation information is often challenging (Shi and Wang, 2021; Xie et al., 2024).

Currently, two-dimensional (2D) stratigraphic profiles are commonly used to guide the design and construction of engineering projects (Guan et al., 2024a; Hu et al., 2024). Selecting representative stratigraphic profiles to comprehensively reflect the spatial distribution of soil properties largely depends on the engineer's experience. For large geotechnical projects with complex geological conditions, detailed three-dimensional (3D) subsurface models are needed to thoroughly characterize

46 the spatial distribution of soil properties (Jiang et al., 2024a; Shi et al., 2023; Shi and Wang, 2022).
47 Additionally, detailed 3D subsurface models can help mitigate uncertainties caused by human factors.
48 Subsurface modelling using interpolation or data-driven methods is an active area of study (Hu et al.,
49 2024; Z. Z. Wang et al., 2023; Yang et al., 2023a, 2023b). The Kriging method, proposed in 1960, has
50 been widely applied for the interpolation of 2D and 3D soil properties (Zou et al., 2017). As a
51 geostatistical model, Kriging infers the properties of unknown points through the weighted averaging
52 of known properties within a certain range, making it an optimal linear unbiased estimator. However,
53 the Kriging method requires the estimation of model parameters to ensure reliability of predictions
54 (Nag et al., 2023). Moreover, when simulating large-scale or high-resolution 3D random fields, the
55 Kriging method may consume substantial computational resources in the storage and processing of
56 large correlation matrices. As a solution, Yang and Ching (2021) applied the conditional random field
57 method to 3D site modeling with reduced computational complexity based on the assumption of
58 separable autocorrelation function. Bayesian Compressive Sensing (BCS), a non-parametric and data-
59 driven method, has also been extensively used for modelling non-stationary processes and fields, but
60 BCS lacks site-specific basis functions for geotechnical modeling (Cami et al., 2020). Alternatively,
61 Xie et al. (2022b) proposed a data-driven modeling method based on geotechnical distance fields, but
62 it has yet to be extended to 3D subsurface modeling cases. Additionally, soil properties exhibit location
63 dependency, and the properties at a given location are only correlated with those at another location
64 within a certain scale of fluctuation (SoF) (Phoon et al., 2003). Therefore, predicting soil properties at
65 unsampled points solely based on correlation distance may overlook this fact.
66 Incorporating domain knowledge, such as random field theory into data-driven machine learning

models is a promising approach (Lyu et al., 2024; Wu et al., 2023). It addresses challenges related to the weak interpretability, poor generalization, and physical inconsistency of machine learning models. For example, Chen et al. (2023) used a large number of 2D synthetic samples derived from random field theory as 'prior' information to generate deep learning models. These models, enriched with prior information, then guided subsurface modeling for site-specific 2D applications. However, generating and storing large numbers of 3D random field synthetic samples and inputting them into models for training is challenging. Furthermore, Chen et al. (2024) used the correlation matrix from random field theory to characterize the spatial positions of soil cells within a site, embedding random field theory into a data-driven model. Nevertheless, calculating the correlation matrix requires additional random field parameters. Estimating these parameters for 3D sites is particularly challenging when borehole data is sparse (Qi et al., 2022; Xiao et al., 2018; J.-Z. Zhang et al., 2022; Zhang et al., 2021). Additionally, the number of soil cells in a 3D site increases significantly compared to a 2D site, making the storage and processing of large correlation matrices time-consuming (Z. Yang et al., 2022). It is worth noting that in geotechnical subsurface modeling, 'prior' information encompasses not only the domain knowledge (random field theory) but also measurement data from neighboring or similar sites (Guan et al., 2024b) and multi-source measurement data (Xie et al., 2022a). This study primarily focuses on embedding random field theory as 'prior' information into data-driven models, which proves particularly beneficial in scenarios where similar measurement data are challenging to obtain.

To address the described issues above, this paper proposes a data-driven framework that uses random field theory to achieve 3D subsurface modeling with reduced computational complexity and no parameters. The framework employs a correlation matrix processed through principal component

analysis (PCA) to characterize the spatial positions of soil cells, providing a rich set of basis functions for subsurface modeling. Additionally, to reduce the computational complexity of processing large correlation matrices with PCA, a strategy is proposed that involves sparse sampling followed by projection into the principal component space. A series of synthetic random field samples are statistically analyzed to investigate the impact of scale of fluctuation on subsurface modeling accuracy, aiming to eliminate correlated parameters. The performance of the proposed method is validated using a large number of synthetic cases and two real case histories. The remainder of this study is organized as follows: Section 2 introduces the proposed enhanced subsurface modeling framework. Section 3 discusses the improvements and simplification strategies of the proposed framework through a series of synthetic cases. Section 4 provides a detailed description of the implementation procedures of the proposed method. Sections 5 and 6 compare and validate the method using both 2D and 3D examples, followed by the conclusion.

2 Proposed Subsurface Modeling Methods

The essence of data-driven subsurface modeling lies in using sparse measurement information to infer soil properties at multiple unmeasured locations. This study aims to integrate random field theory into data-driven models through Geotechnical Correlation Fields (GCFs) to reduce uncertainty in subsurface modeling and enhance model reliability.

2.1 Three-dimensional Geotechnical Correlation Field

The geological and environmental processes during soil deposition result in spatial variability in near-surface soils. Random Field Theory (RFT), as a powerful tool for evaluating the spatial variability of soil properties, is widely used for modeling the inherent variability of soils (Stuedlein et al., 2012a).

RFT adheres to the fact that soil properties at a given site exhibit spatial dependency, meaning that soil properties are correlated only within a certain lag distance. In RFT, the inherent variability of soil properties is described not only by mean and variance but also by autocorrelation functions (ACFs) and scales of fluctuation (SoF) (Cami et al., 2020). Eq. (1) demonstrates a commonly used ACF—the Single Exponential (SNX) model. ACFs quantify the correlation $\rho_{i,j}$ between soil cells i and j, rather than relying solely on the distance between them. It is important to note that before implementing RFT, the site must be discretized into N soil cells (cubic elements) based on engineering requirements, with each cell assumed to be homogeneous internally.

$$\rho_{i,j} = \exp\left[-2\left(\frac{|\tau_{i,j}^{x}|}{SOF_x} + \frac{|\tau_{i,j}^{y}|}{SOF_y} + \frac{|\tau_{i,j}^{z}|}{SOF_z}\right)\right] \quad (i,j \in [1,N]) \tag{1}$$

where $\tau_{i,j}^{x}$, $\tau_{i,j}^{y}$, and $\tau_{i,j}^{z}$ represent the distances between soil cells i and j along the x-, y-, and z-axis directions, respectively. SoF_x, SoF_y, and SoF_z correspond to the scales of fluctuation for a specific site in the x-, y-, and z-axis directions. Table A1 in Appendix A presents seven common types of ACFs (Cami et al., 2020; Ching et al., 2019).

To calculate the correlation ρ between every pair of soil cells, a correlation matrix $\mathbf{C}$ of dimension $N \times N$ is constructed, as shown in Eq. (2). In this matrix, $\rho_{i,j} = 1$ when i=j, and $\mathbf{C}$ is symmetric ($\rho_{i,j} = \rho_{j,i}$). The first row of $\mathbf{C}$, denoted as $\mathbf{CV}_1$, represents the correlation vector between the first soil cell and all other soil cells. Using $\mathbf{CV}_1$, the relative spatial position of the first soil cell within the site can be expressed. Similarly, the relative spatial positions of the remaining soil cells can be represented as $\mathbf{CV}_i (i \in [1,N])$. As shown in Fig. 1(a), the correlation vectors for soil cells A–E are illustrated for the case where SoF_x and SoF_y=100 m, and SoF_z=1.0 m. The correlation decreases as the distance from soil cells A–E increases, indicating that soil properties exhibit correlation only within the scale of

fluctuation.

$$\mathbf{C}_{N\times N}=\begin{bmatrix}\rho_{1,1} & \rho_{1,2} & \cdots & \rho_{1,j} & \cdots & \rho_{1,N}\\ \rho_{2,1} & \rho_{2,2} & \cdots & \rho_{2,j} & \cdots & \rho_{2,N}\\ \cdots & \cdots & \cdots & \cdots & \cdots & \cdots\\ \rho_{i,1} & \rho_{i,2} & \cdots & \rho_{i,j} & \cdots & \rho_{i,N}\\ \cdots & \cdots & \cdots & \cdots & \cdots & \cdots\\ \rho_{N,1} & \rho_{N,2} & \cdots & \rho_{N,j} & \cdots & \rho_{N,N}\end{bmatrix}=\begin{bmatrix}\mathbf{CV}_1\\ \mathbf{CV}_2\\ \cdots\\ \mathbf{CV}_i\\ \cdots\\ \mathbf{CV}_N\end{bmatrix}(i,j\in[1,N]) \quad (2)$$

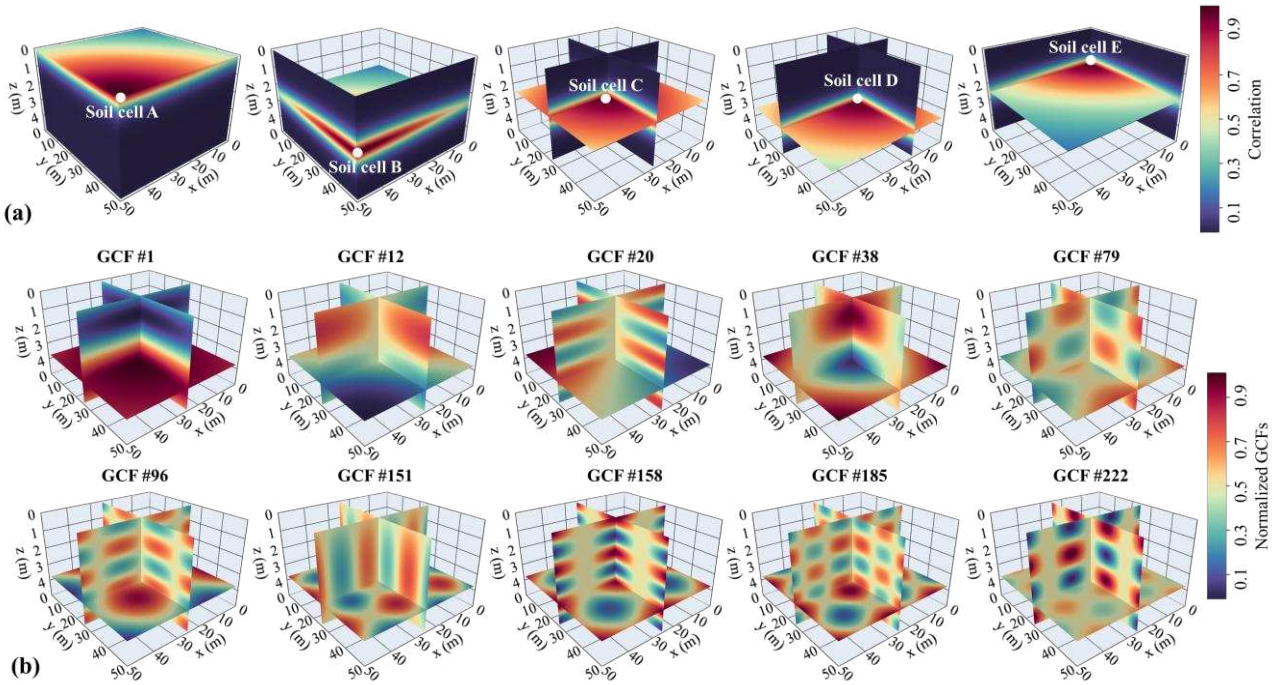

Fig. 1 Visual representation of the 3D correlation matrix and geotechnical correlation fields: (a) Correlation of soil cells A–E with all other soil cells (SoF$_x$ and SoF$_y$=100 m, and SoF$_z$=1.0 m); (b) Forms of geotechnical correlation fields (GCFs) corresponding to different principal components. Note: Each GCF has been normalized to a range of 0–1.

Conventional subsurface modeling methods such as conditional random fields or Kriging often require operations like matrix inversion of the correlation matrix **C**, which can be computationally intensive when N (the number of soil cells) is large. A simplified approach proposed by Chen et al. (2024) involves the following steps: ① Data Collection: Gather measured soil cell properties $q_i(i\in$ [measured cells]) and their corresponding correlation vectors $\mathbf{CV}_i$; ② Data-Driven Modeling: Use a data-driven model to establish a complex nonlinear relationship between $\mathbf{CV}_i$ and q_i. ③Prediction:

Apply the trained data-driven model to predict the properties of unmeasured soil cells.

It is important to note that soil properties are only correlated within the range of the scale of fluctuation, leading to a sparse matrix with many zero elements in $\mathbf{C}$. Therefore, directly using the correlation vector $\mathbf{CV}_i$ as input features for the data-driven model is not ideal. This approach may result in excessively high input dimensions with a significant number of redundant zero features, which can substantially reduce both the training and prediction efficiency of the model. To address this issue, this study first applies dimensionality reduction to $\mathbf{C}$ using Principal Component Analysis (PCA). The top k eigenvectors with the largest eigenvalues are used to represent $\mathbf{P}_{\mathbf{C}_{(N\times k)}}$, as shown in Eq. (2). Since k is much smaller than N, $\mathbf{P}_{\mathbf{C}_{(N\times k)}}$ is easier to store compared to the original correlation matrix $\mathbf{C}_{N\times N}$. In this study, $\mathbf{P}_{\mathbf{C}_{(N\times k)}}$ is referred to as the geotechnical correlation field, which encapsulates the main information from the correlation matrix.

$$\mathbf{P}_{\mathbf{C}_{(N\times k)}} = \mathrm{PCA}(\mathbf{C}_{N\times N}) = \begin{bmatrix} P_{1,1} & P_{1,2} & \cdots & P_{1,k} \\ P_{2,1} & P_{2,2} & \cdots & P_{2,k} \\ \cdots & \cdots & \cdots & \cdots \\ P_{i,1} & P_{i,2} & \cdots & P_{i,k} \\ \cdots & \cdots & \cdots & \cdots \\ P_{N,1} & P_{N,2} & \cdots & P_{N,k} \end{bmatrix} = \begin{bmatrix} \mathbf{PV}_1 \\ \mathbf{PV}_2 \\ \cdots \\ \mathbf{PV}_i \\ \cdots \\ \mathbf{PV}_N \end{bmatrix} (i \in [1, N]) \quad (2)$$

As shown in Fig. 1(b), ten geotechnical correlation fields (GCFs) of a specific site are presented, highlighting the significant differences in the forms of different GCFs. GCF #1($[P_{1,1}, P_{2,1}, \cdots, P_{N,1}]^{\mathrm{T}}$), representing the geotechnical correlation field corresponding to the first principal component, exhibits relatively smooth variations in the *xz* and *yz* planes. Compared to GCF #1, GCF #12 shows notable distinctions in the *xy* plane, while GCF #20 exhibits more complex fluctuations in the *xz* and *yz* planes relative to GCF #12. Overall, the complexity of GCFs increases with the growth of k. Consequently, GCFs effectively capture the spatial variability of soil properties within the site, encompassing both

low-frequency and high-frequency information. Additionally, the diverse forms of GCFs offer a robust set of basis functions for accurately characterizing spatial variations of soil properties.

2.2 Simplified Strategy for Generating 3D GCFs

GCFs effectively address the challenges of low computational efficiency in data-driven models caused by the sparsity and high dimensionality of the original correlation matrix. Additionally, GCFs provide diverse basis functions for data-driven subsurface modeling and embed random field theory knowledge into the input features of the model. However, for large-scale or high-resolution 3D sites, the number of soil cells N can reach tens of thousands. Directly processing such massive correlation matrices to obtain GCFs can be exceedingly time-consuming. Therefore, it is necessary to propose a simplified approach to enhance the efficiency of GCF generation, thereby expanding the applicability of GCF-based data-driven subsurface modeling methods.

(1) Simplifying 3D GCFs into a Combination of 2D GCFs on *xy*, *xz*, and *yz* Planes

As shown in Fig. 2(a), horizontal scale of fluctuations in geotechnical sites are typically larger, ranging from 5 to 105 m, while vertical scale of fluctuations are relatively smaller, between 0.1 and 3.1 m (Chen et al., 2023). Figs. 2(d)-(e) illustrate two 3D GCFs generated with SoF_x and SoF_y=100 m, and SoF_z=1.0 m. Interestingly, directly calculating GCFs on the *xy* plane and the *xz*/*yz* 2D planes yields GCFs with cross-sectional forms consistent with those of the 3D GCFs. This observation indicates that 3D GCFs essentially represent a superposition of a series of 2D GCFs.

Therefore, this study adopts a combination of GCFs from the *xy*, *xz*, and *yz* planes to represent the spatial positions of soil cells in 3D space, referencing the representation of (x, y, z) coordinates in 3D Euclidean space, as shown in Fig. 2(b). This approach eliminates the need for direct generation and

processing of large correlation matrices in 3D sites, substituting them with more manageable 2D planes.

To do so, the GCFs for the *xy*, *yz*, and *xz* planes are calculated separately. The projection points for soil cell *i* in these three planes (denoted as points A, B, and C in Fig. 2(c)) are identified. Combining the GCFs of the projection points from the three planes, the representation of the soil cell is obtained in 3D space as $\{[P_{A,1}, P_{A,2}, \cdots, P_{A,k1}]$ & $[P_{B,1}, P_{B,2}, \cdots, P_{B,k2}]$ & $[P_{C,1}, P_{C,2}, \cdots, P_{C,k3}]\}$, where $k1$, $k2$, and $k3$ represent the number of principal components retained in the *xy*, *yz*, and *xz* planes. The values of k for different planes are discussed in Section 3.2.

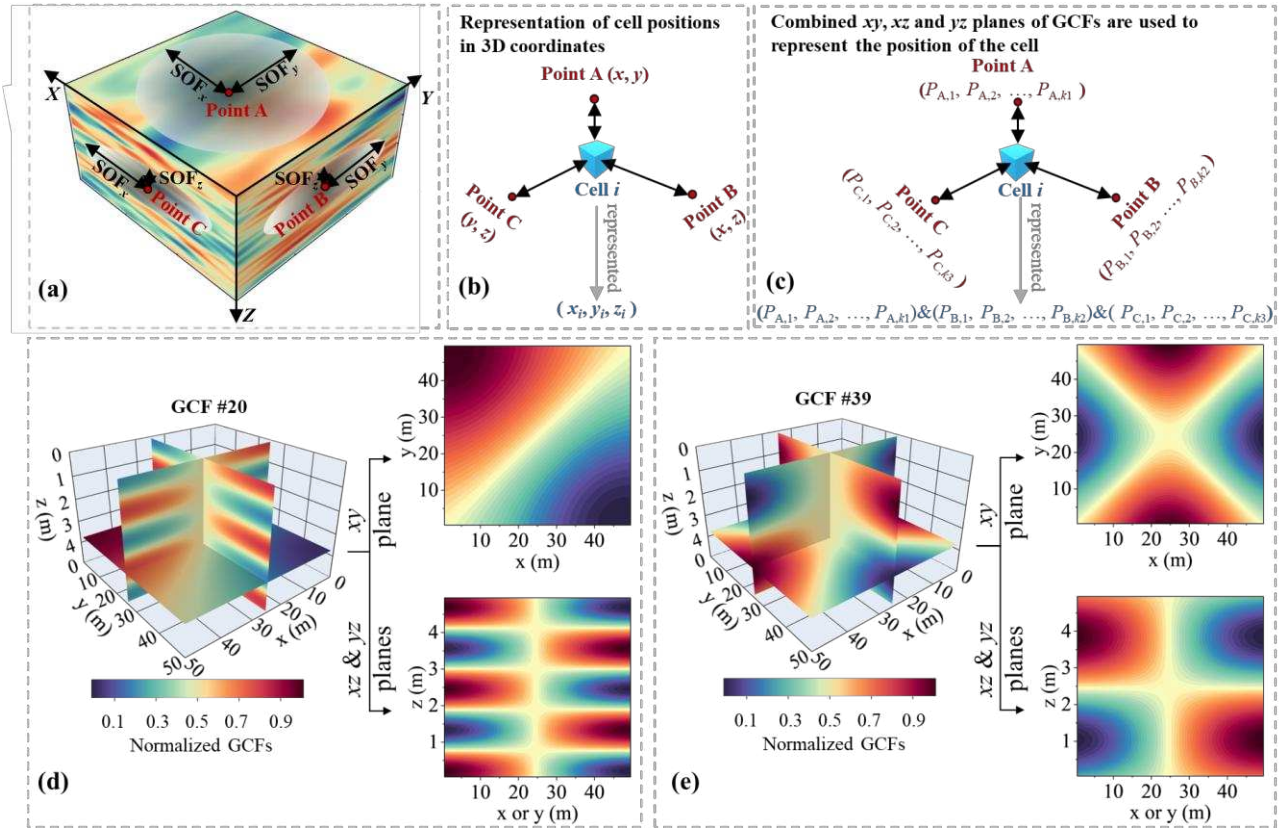

Fig. 2 Transforming 3D GCFs into a combination of 2D GCFs: (a) Schematic of a 3D geotechnical site and its SoFs; (b) Representation of soil cell spatial positions using 3D coordinates; (c) Representation of soil cell spatial positions using a combination of GCFs on the *xy*, *xz*, and *yz* planes; (d)-(e) Decomposition of 3D GCFs into GCFs on the *xy*, *xz*, and *yz* planes.

(2) Reducing the Computational Complexity of GCFs via Sparse Sampling

It is worth noting that simplifying 3D GCFs into a combination of GCFs on the *xy*, *xz*, and *yz*

planes, can effectively improve the efficiency of GCF generation. However, in large-scale or high-resolution sites, the number of soil cells in a 2D plane remains substantial, making subsequent PCA operations computationally challenging. Therefore, this study proposes a sparse sampling strategy to reduce the computational complexity of generating 2D GCFs. For clarity, Fig. 3 illustrates the process of generating GCFs and subsurface modeling using the *xy*-plane. Similar processes repeat for the *xz* and *yz* planes. The key steps are summarized as follows:

Simplified Step 1: Divide the site into N soil cells according to the requirements of the engineering project.

Simplified Step 2: A total of G soil cells are sampled at regular intervals from the N total cells, referred to as GCFs cells. The impact of the sampling interval is discussed in Section 3.1.

Simplified Step 3: As shown in Eqs. (3) and (4), the correlation matrix $\mathbf{C}_{N\times G}$ is computed for the N soil cells and the sampled G cells, resulting in an $N\times G$ dimensional matrix. Simultaneously, the correlation matrix $\mathbf{C}_{G\times G}$ for the G soil cells is calculated, yielding a $G\times G$ dimensional matrix. It is noteworthy that both $\mathbf{C}_{N\times G}$ and $\mathbf{C}_{G\times G}$ have lower dimensions than $\mathbf{C}_{N\times N}$, which facilitates storage.

$$\mathbf{C}_{N\times G}=\begin{bmatrix}\rho_{1,1} & \rho_{1,2} & \cdots & \rho_{1,j} & \cdots & \rho_{1,G}\\ \rho_{2,1} & \rho_{2,2} & \cdots & \rho_{2,j} & \cdots & \rho_{2,G}\\ \cdots & \cdots & \cdots & \cdots & \cdots & \cdots\\ \rho_{i,1} & \rho_{i,2} & \cdots & \rho_{i,j} & \cdots & \rho_{i,G}\\ \cdots & \cdots & \cdots & \cdots & \cdots & \cdots\\ \rho_{N,1} & \rho_{N,2} & \cdots & \rho_{N,j} & \cdots & \rho_{N,G}\end{bmatrix}(i\in[1,N],j\in[1,G]) \tag{3}$$

$$\mathbf{C}_{G\times G}=\begin{bmatrix}\rho_{1,1} & \rho_{1,2} & \cdots & \rho_{1,j} & \cdots & \rho_{1,G}\\ \rho_{2,1} & \rho_{2,2} & \cdots & \rho_{2,j} & \cdots & \rho_{2,G}\\ \cdots & \cdots & \cdots & \cdots & \cdots & \cdots\\ \rho_{i,1} & \rho_{i,2} & \cdots & \rho_{i,j} & \cdots & \rho_{i,G}\\ \cdots & \cdots & \cdots & \cdots & \cdots & \cdots\\ \rho_{G,1} & \rho_{G,2} & \cdots & \rho_{G,j} & \cdots & \rho_{G,G}\end{bmatrix}(i,j\in[1,G]) \tag{4}$$

where $\rho_{i,j}$ represents the correlation between the i-th and j-th soil cells, which is calculated using the ACFs and the corresponding SoFs. The detailed calculation formula can be found in Table A1 of

Appendix A. However, accurately determining these parameters is challenging in the presence of sparse survey information (Qi et al., 2022; Xiao et al., 2018; Zhang et al., 2021). Section 3.2 provides a detailed discussion on the impact of these parameters.

Simplified Step 4 & 5: PCA is applied to $\mathbf{C}_{G\times G}$ to obtain a projection matrix with k principal components. Subsequently, $\mathbf{C}_{N\times G}$ is projected onto the selected k principal components, resulting in an $N\times k$ dimensional $\mathbf{P}_{\mathbf{C}(N\times k)}$ matrix, as shown in Eq. (5). Notably, this approach significantly reduces computational complexity compared to directly performing PCA on the $\mathbf{C}_{N\times N}$, especially when N is large. The PCA operations are implemented using Python's scikit-learn v1.1.3 (Pedregosa et al., 2018). Further discussion can be found in Section 3.1.

$$\mathbf{P}_{\mathbf{C}(N\times k)} = \mathbf{C}_{N\times G} \times (\mathrm{PCA}(\mathbf{C}_{G\times G}))_{G\times k}\ (i \in [1, N]) \tag{5}$$

Simplified Step 6: Determine the survey locations and collect the measured CPT results q (e.g., cone tip resistance, sleeve friction) or other soil parameters (e.g., penetration pore water pressure, undrained shear strength). The measured properties of n soil cells are used to form the training set, while the remaining m (m=N−n) soil cells, with unknown properties, form the test set. The input features of the training set (i.e., $N\times k$ matrix) are the row vectors corresponding to n soil cells in the $\mathbf{P}_{\mathbf{C}}$ matrix, and the outputs are the measured values of the soil properties for n soil cells. A data-driven model is used to learn the nonlinear relationship between the input features and outputs in the training set. Once trained, the model can be used to predict the properties of m unsampled soil cells. This study integrates random field theory into the data-driven model through input features, making the proposed method highly flexible and applicable to any data-driven model. The Shortcut-Connected Neural Network (SCNN) and the Extra Trees (ET) models are adopted and compared. A detailed description

of the SCNN and ET models is provided in Appendix B.

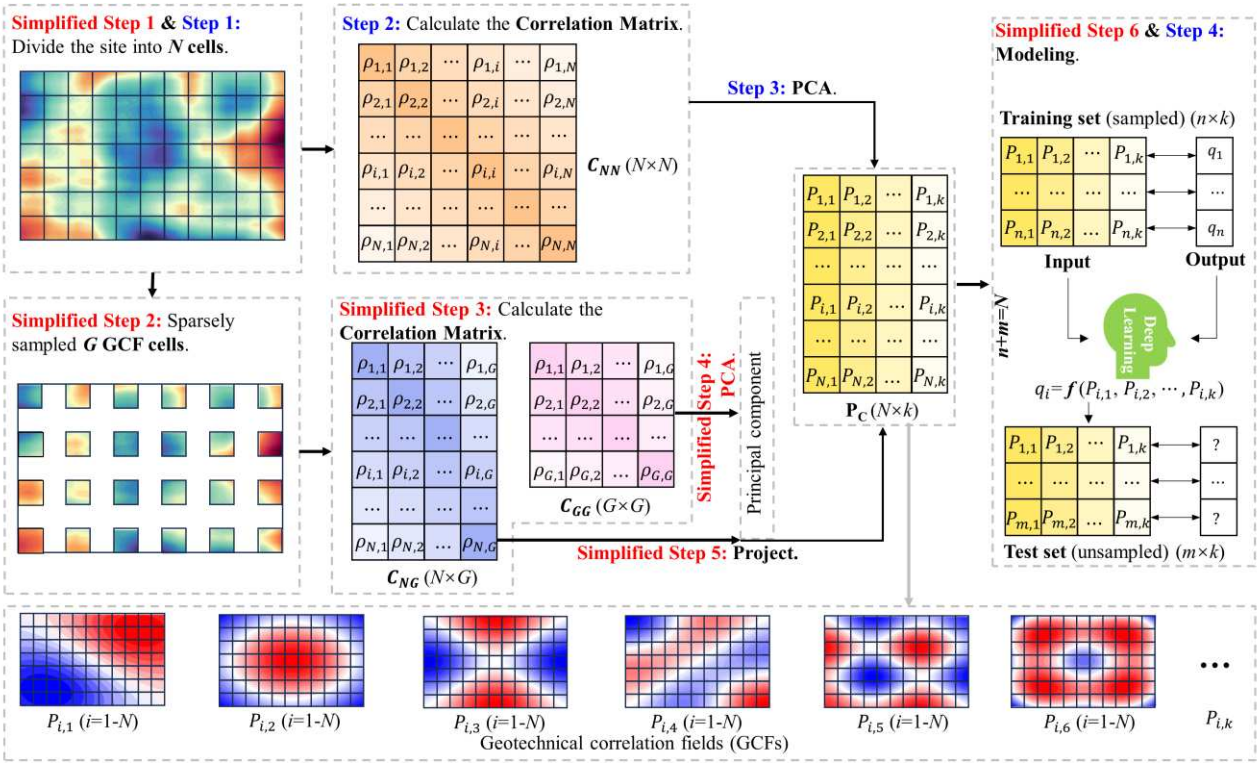

Fig. 3 Process of generating GCFs and performing subsurface modeling, illustrated using the *xy*-plane as an example.

2.3 Characterization of Uncertainty in Subsurface Modeling

The task of subsurface modeling requires inferring soil properties at unmeasured locations based on sparse measurement data. Typically, the number of soil cells in unknown areas far exceeds the number of measured cells, leading to significant uncertainties in the subsurface modeling results. Accurate quantification of the uncertainty in subsurface modeling is crucial for guiding the investigation and design processes in geotechnical engineering (Yan et al., 2023; Zhang et al., 2024; C. Zhao et al., 2023). Prioritizing investigation points in areas of high uncertainty can effectively reduce the uncertainty of the subsurface model and mitigate the risk of geotechnical disasters caused by spatial variability in soil properties.

The data-driven models used in this study are the ET model and the SCNN model. The ET model,

as an ensemble learning method, approximates the true hypothesis by combining multiple weak learners. A common strategy to quantify the predictive uncertainty of ensemble learning models is to perform statistical analysis on the multiple weak learners (Xie et al., 2022a). According to the central limit theorem, the resampling distribution of the predicted values will approximate a gaussian distribution. The standard deviation (σ) of the predictions from all weak learners can be used to estimate the uncertainty of the prediction results:

$$\sigma = \sqrt{\frac{\sum_{i=1}^{n}\left[f_{\mathrm{ET}}^{i}(\mathbf{PV}) - \overline{f_{\mathrm{ET}}}\right]^2}{n-1}} \tag{6}$$

where $f_{\mathrm{ET}}^{i}(\mathbf{PV})$ is the prediction result from the i-th weak learner; $\overline{f_{\mathrm{ET}}}$ is the average prediction result from the n weak learners,

For the SCNN model, uncertainty can be quantified using Monte Carlo dropout (MC dropout) and random weight initialization methods to quantify uncertainty in model predictions. MC dropout operates by randomly disconnecting a certain proportion of neural connections, resulting in an altered model architecture (T. Wang et al., 2023; P. Zhang et al., 2022). Given that the model architecture changes each time, the standard deviation of the predictions after performing t Monte Carlo dropout sampling runs can be calculated as follows:

$$\sigma = \sqrt{\frac{\sum_{i=1}^{t}\left[f_{\mathrm{SCNN}}^{i}(\mathbf{PV}, \mathrm{dropout}(\mathbf{W}, \mathbf{b})) - \overline{f_{\mathrm{SCNN}}}\right]^2}{t-1}} \tag{7}$$

where $\mathbf{W}$ and $\mathbf{b}$ are the weights and biases of the neural network; $\mathrm{dropout}(\mathbf{W}, \mathbf{b})$ refers to randomly deactivating a portion of the neural connections during the t-th prediction, effectively altering the network's architecture and introducing variability; $f_{\mathrm{SCNN}}^{i}(\mathbf{PV}, \mathrm{dropout}(\mathbf{W}, \mathbf{b}))$ represents the prediction result from the i-th random forward pass of the network, where dropout is applied each time;

271 $\overline{f_{\mathrm{SCNN}}}$ is the mean prediction result across all t forward passes (predictions). The MC dropout method
272 is simple and efficient. However, the uncertainty in prediction results is often closely related to the
273 design of the dropout structure, such as the dropout rate and the number of dropout layers.
274 Consequently, selecting an appropriate dropout structure generally requires engineers to have
275 substantial experience and time to conduct repeated trials.

276 The random weight initialization method does not require any additional user-defined parameters.
277 It introduces variability into the model by assigning different initial trainable parameters to the neural
278 network, causing the model to follow different optimization paths during the iterative optimization
279 process. As a result, this method generates different predictions based on the distinct paths taken by
280 the model. However, the random weight initialization method requires training m neural networks,
281 each with different initial parameters. This can be computationally expensive, particularly for complex
282 models that are time-consuming to train. The uncertainty in the prediction results can be represented
283 as:

284 $$\sigma = \sqrt{\frac{\sum_{i=1}^{m}\left[f_{\mathrm{SCNN}}^{i}(\mathbf{PV}, \mathbf{W}_i, \mathbf{b}_i) - \overline{f_{\mathrm{SCNN}}}\right]^2}{m-1}} \tag{8}$$

285 where $\mathbf{W}_i$ and $\mathbf{b}_i$ are the weights and biases of the i-th neural network; $f_{\mathrm{SCNN}}^{i}(\mathbf{PV}, \mathbf{W}_i, \mathbf{b}_i)$ represents
286 the prediction from the i-th neural network, trained with different initial parameters; $\overline{f_{\mathrm{SCNN}}}$ is the
287 average prediction result from the m networks. It is important to note that the SCNN model structure
288 employed in this study is relatively simple and easy to train. Therefore, random weight initialization
289 is employed to quantify uncertainty in subsurface modeling.

290 **2.4 Model Interpretability**

291 Regarding deep learning for geotechnical engineering, the relationship between inputs and outputs

remains difficult to analyze and interpret. SHapley Additive exPlanations (SHAP) is a game-theory-based method for interpreting black-box models. This study uses SHAP to interpret the ET and SCNN models used for subsurface modeling, providing deeper insights into the model's internal mechanisms and evaluating the contribution of each input feature (i.e., GCFs) to the random field predictions. SHAP method avoids the necessity of heuristically selecting methods to linearize components. Instead, it derives an effective linearization directly from the SHAP values calculated for each component (Lundberg and Lee, 2017).

The TreeSHAP method can be used to interpret the output of the ET model and measure the importance of each dimension of the GCFs in contributing to the subsurface modeling results. Similarly, for the SCNN model, the DeepSHAP method, which is specifically designed for deep learning models, can be applied to explain the model's predictions. In both cases, these methods provide a way to quantify the contribution of each dimension of the GCFs to the final model output. This is particularly useful for understanding the underlying factors driving the predictions of complex models, where interpretability is crucial for ensuring model reliability and trustworthiness. By using TreeSHAP and DeepSHAP for SCNN models, it is possible to gain insight into how different GCFs, as well as their individual components, influence the model's predictions, and identify which features are most important for making accurate subsurface predictions. This study uses the Python-based SHAP library v0.46.0 (Lundberg and Lee, 2017) for model interpretation.

2.5 Evaluation Metrics

Three types of evaluation metric are employed to assess the accuracy of subsurface modeling: (1) R-squared (R^2) is used to evaluate the goodness of fit, with values closer to 1 indicating better model

performance (see Eq. (7)); (2) the root mean square error (*RMSE*) is used to evaluate the model's error from the perspective of absolute error (see Eq. (8)); (3) the mean absolute percentage error (*MAPE*) is employed to assess model accuracy from the perspective of relative error (see Eq. (9)). It is important to note that when the measured value (e.g., cone tip resistance) of a soil cell is close to zero, *MAPE* may not adequately assess the model's performance. Therefore, the symmetric mean absolute percentage error (*sMAPE*) is introduced as a supplementary metric (see Eq. (10)).

$$R^2 = 1 - \frac{\sum_{i=1}^{N}(q_i - \hat{q}_i)^2}{\sum_{i=1}^{N}(q_i - \bar{q})^2} \tag{7}$$

$$RMSE = \sqrt{\frac{1}{N}\sum_{i=1}^{N}(q_i - \hat{q}_i)^2} \tag{8}$$

$$MAPE = \frac{1}{N}\sum_{i=1}^{N}\left|\frac{q_i - \hat{q}_i}{q_i}\right| \times 100\% \tag{9}$$

$$sMAPE = \frac{1}{N}\sum_{i=1}^{N}\frac{|q_i - \hat{q}_i|}{(q_i + \hat{q}_i)/2} \times 100\% \tag{10}$$

where N is the total number of soil cells; q_i and $\hat{q}_i$ are the measured and predicted properties of soil cell i.

3 Validation of two simplified strategies

A set of synthetic zero-mean stationary gaussian random fields with different horizontal and vertical SoF are used to illustrate the performance and sensitivity of the proposed method with the special focus on the following aspects: (1) how to sample as few soil cells as possible to generate accurate GCFs, bypassing the storage of large correlation matrices and reducing the computational complexity of PCA; (2) the impact of RFT parameters on subsurface modeling. The synthetic 3D site spans 100 m horizontally (x and y) and has a depth (z) of 10 m. The site is simulated with resolutions

of 1.0 m horizontally and 0.1 m vertically. The mean (μ) and stand deviation (σ) of the synthetic samples are set as 11 MPa and 3 MPa, respectively. The horizontal SoFs of the synthetic data are 10, 30, 50, 70, and 90 m, while the vertical SoFs are 0.1, 0.5, 1.0, 1.5, and 2.0 m. For each combination of SoFs, 50 samples are randomly simulated using the Cholesky decomposition method (Y. Yang et al., 2022), yielding a total of 3,750 synthetic samples.

3.1 Reducing the Computational Complexity of GCF Generation

This study uses a combination of three 2D-plane GCFs (*xy*, *xz*, and *yz*) to represent the spatial locations of soil cells within a 3D site. Since there is no essential difference between the *yz* and *xz* planes, only the *xy* and *xz* planes are analyzed in subsequent steps. To avoid redundancy, the SoF values in the x and y directions are set to 100 m, and the SoF in the z direction is set to 0.5 m for the presentation. For detailed procedures, see Section 2.2.

As shown in Fig. 4 (a), a comparison is made between the GCFs generated using all soil cells (first row) and those generated with a sampling interval of 10 m (second row). The GCFs are arranged in order of decreasing eigenvalue as part of the PCA operation. It is observed that the GCFs exhibit an increasing trend in complexity from front to back. Furthermore, the GCFs generated using the sparse sampling strategy demonstrate a high degree of consistency with the original GCFs. It is worth noting that each GCF is normalized to ensure it remains within the gradient-sensitive range of the neural network, thus accelerating the model's training process. Some of the simplified GCFs exhibit values that are inversely related to those of the original GCFs. However, this does not affect the ML model's performance.

As shown in Fig. 4(b), the GCFs generated using all soil cells (first row) closely resemble those

produced with a 0.2 m sampling interval in the z direction (second row). However, when a 0.5 m sampling interval is applied in the z direction, the generated GCFs exhibit noticeable striping. This phenomenon is primarily due to the site's SoF in the z direction being set at 0.5 m. Therefore, the sampling interval must be smaller than the SoF of the site. Additionally, there are significant differences in the morphology of GCFs between the xz and xy planes. The first 20 GCF components in the xz plane resemble vertical waves, with progressively shorter periods and higher frequencies as the components advance. Beyond the 21st component, the GCFs resemble overlapping transverse and vertical waves, with an increasing frequency. These diverse GCF components will serve as basis functions, providing a robust foundation for subsequent subsurface modeling.

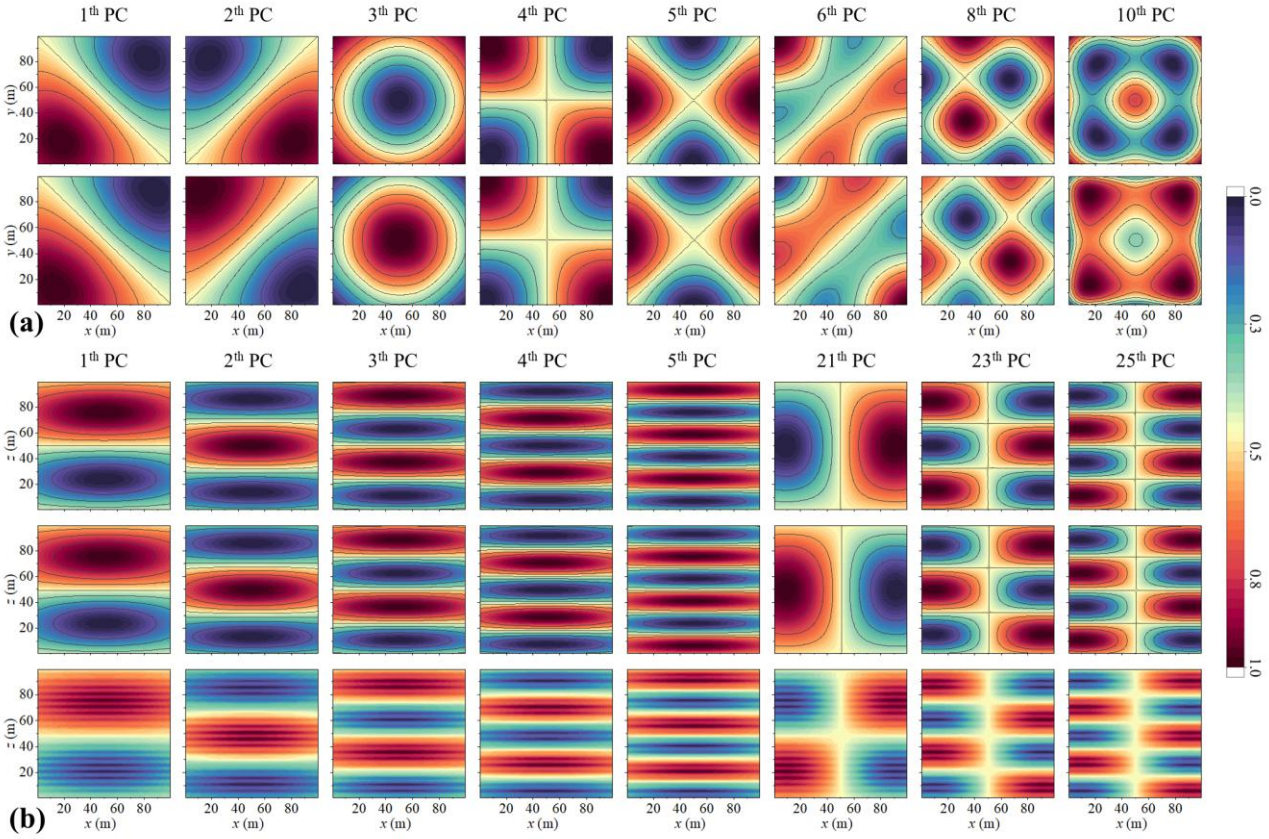

Fig. 4 Performance of generating GCFs using the simplified strategy: (a) Morphology of GCFs at different sampling intervals when the SoFs in the x and y directions of the xy plane are set to 100 m, with the first row showing the original GCFs and the second row showing the simplified GCFs at a

10 m sampling interval; (b) Morphology of GCFs when the SoFs in the x and z directions of the xz plane are set to 100 m and 0.5 m, respectively, with the first row showing the original GCFs and the second and third rows showing the simplified GCFs at sampling intervals of 0.2 m and 0.5 m.

Fig. 5 illustrates the performance of generating GCFs using soil cells with different sampling intervals in the xy plane. It can be observed that when the sampling intervals in the x and y directions are set between 2 and 10 m, the GCFs generated using the simplified strategy show a high similarity to those generated using all soil cells, with an R^2 value approaching 1. When the sampling interval exceeds 15 m, the accuracy of the GCFs generated using the simplified strategy gradually decreases, leading to increased uncertainty. Therefore, it is recommended that the sparse sampling interval for generating the GCFs in the xy-plane should be smaller than 0.1 times the SoF_x or SoF_y. It is noteworthy that generating GCFs directly using all soil cells (10,000 in total) requires the PCA to process a 10,000 × 10,000 correlation matrix. However, when the sampling interval is set to 10 m, only 121 soil cells are available, requiring PCA to process a correlation matrix of size 121 × 121. This significantly reduces the computational complexity of the PCA operation and confines the generation time of the GCFs to approximately 0.02 s.

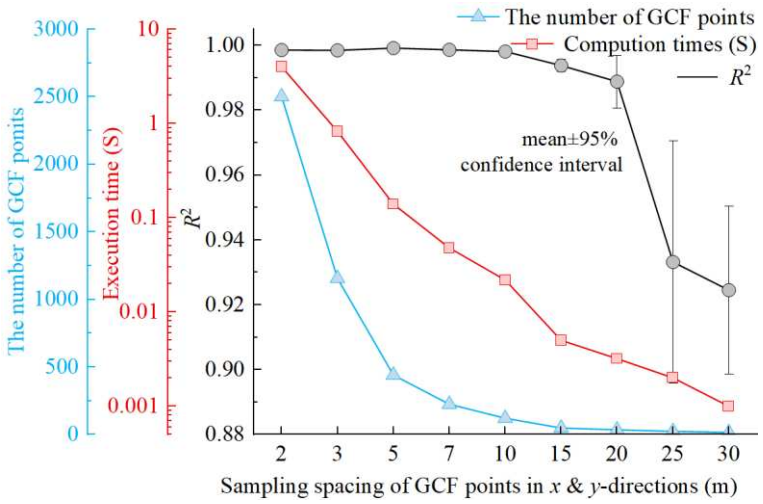

Fig. 5 Impact of different sampling intervals in the x and y directions on the performance of GCFs

generated in the *xy* plane.

As shown in Fig. 6, the performance of generating GCFs using soil cells with different sampling intervals in the *xz* plane is evaluated. Given that sampling in the *x* direction at 10 m intervals in the *xy* plane has minimal impact on the accuracy of the generated GCFs, the sampling interval in the *x* direction is fixed at 10 m for this analysis. It can be observed that when the sampling interval in the *z* direction is between 0.2 and 0.3 m, the GCFs generated closely resemble those produced using all soil cells, with an R^2 value approaching 1. However, when the sampling interval exceeds 0.3 m, the accuracy of the simplified GCFs declines rapidly. Therefore, it is recommended that the sparse sampling interval for generating the GCFs in the *xz* and *yz* planes should be smaller than 0.6 times the SoF_z. When the interval is smaller than the resolution in the *z*-direction of the site, no sparse sampling should be performed. Notably, only 550 GCF cells are used when the sampling interval in the *x* direction is 10 m and in the *z* direction is 0.2 m. This significantly reduces the size of the correlation matrix and confines the generation time of the GCFs to approximately 0.2 s.

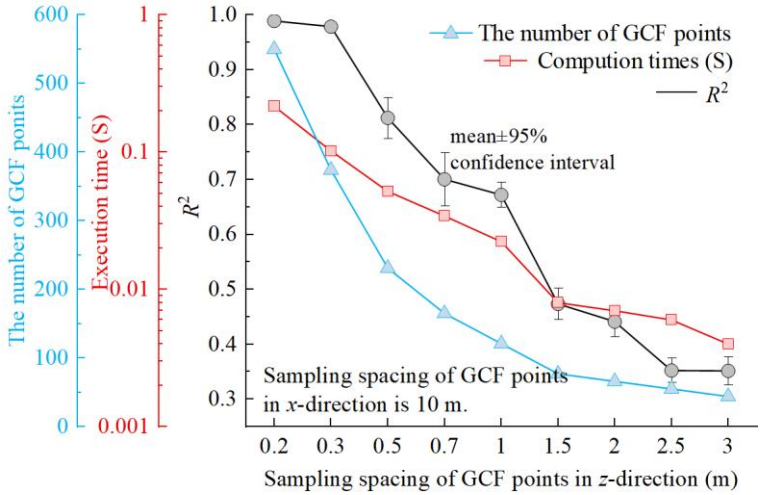

Fig. 6 Effect of different sampling intervals in the *z* direction on the performance of GCFs generated in the *xz* plane

3.2 Impact of RFT Parameters on Subsurface Modeling Results

The GCFs generation process is controlled by random field theory. Therefore, it is necessary to investigate the influence of RFT parameters (SoF and ACF type) on subsurface modeling. To achieve this, a series of *xy* and *xz* sections with different combinations of SoFs are extracted from synthetic 3D samples. Each SoF combination is randomly sampled 50 times. In the *xy* plane, 25 measurement points are arranged at grid points corresponding to *x* and *y* coordinates of 0.5 m, 25.5 m, 50.5 m, 75.5 m, and 99.5 m. In the *xz* plane, 5 boreholes are arranged along sample paths corresponding to *x* coordinates of 0.5 m, 25.5 m, 50.5 m, 75.5 m, and 99.5 m.

(1) The impact of SoFs on modeling accuracy

As shown in Figs. 7(a) and (b), different SoF_x and SoF_z values are used to generate GCFs and perform subsurface modeling. For brevity, only 500 sets of the synthetic field with an SoF_x of 50 m are presented. To eliminate the impact of other factors on modeling accuracy, the GCF dimensions used for the *xy* and *xz* planes are set to 50 and 300, respectively.

For the *xy* plane, the modeling error (RMSE) decreases as the SoF_x used for generating GCFs increases, up to the SoF_x of 50 m. This indicates that in the sparsely measured *xy* plane, using a larger SoF to generate GCFs is beneficial, as it allows more measured data to be used for inferring the properties of unsampled locations. Therefore, selecting a horizontal SoF as 2 times the borehole spacing is a more general choice. Additionally, the horizontal SoF can be treated as a hyperparameter and optimized using a cross-validation method to ensure the rationality of the generated GCFs.

Additionally, it can be observed that as the true scale of fluctuation at the site increases, the spatial variability of soil properties becomes smoother, and the modeling error decreases. For the *xz* plane, the

modeling error increases as SoF_z increases. Using a larger SoF_z to generate GCFs results in predictions that reflect the average trend of the site, thus reducing prediction accuracy. However, given that measurement data in the *z* direction are abundant, using a smaller SoF_z to generate GCFs and perform subsurface modeling is reasonable. This approach helps to accurately reflect the spatial variability of soil properties with depth. Overall, setting SoF_z equal to the resolution of the site in the *z* direction is statistically the optimal choice for generating GCFs.

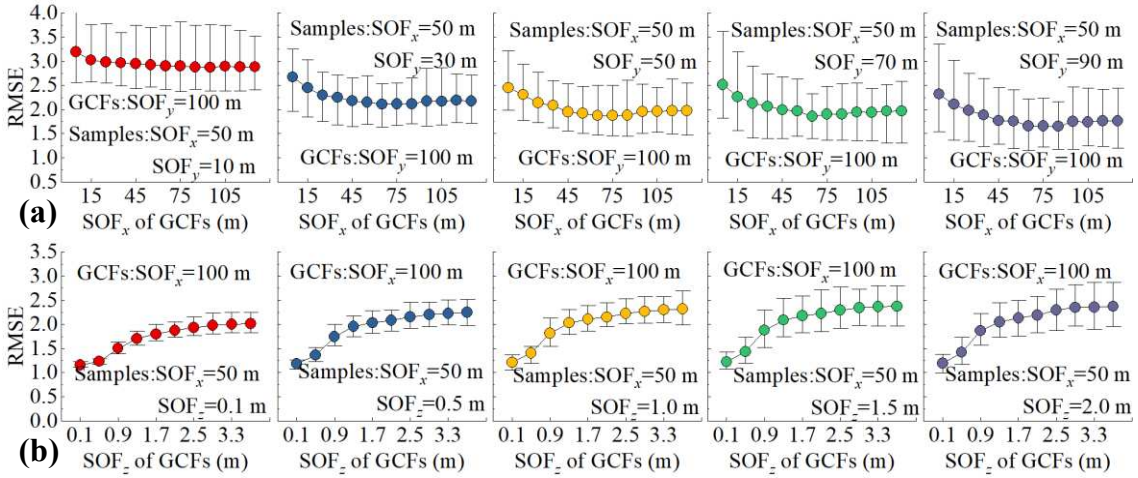

Fig.7 Impact of SoF used to generate GCFs on subsurface modelling results: (a) The impact of different SoF_x values on the modeling accuracy of the *xy* plane. (b) The impact of different SoF_z values on the modeling accuracy of the *xz* plane.

(2) Impact of GCFs dimension on modeling accuracy

Figs. 8(a) and (b) illustrate the impact of using different numbers of GCFs (i.e. PCAs) on the accuracy of subsurface modeling in the *xy* and *xz* planes. To avoid redundancy, only 500 synthetic cases with SoF_x of 70m are shown. For clarity and comparison with Fig. 4, the SoFs used to generate GCFs are consistent with those in Section 3.1. As shown in Fig. 8(a), the error in subsurface modeling results decreases gradually with the increase in the number of GCFs. Specifically, when SoF_y is large, the accuracy of subsurface modeling is sufficiently high even with a small number of GCFs.

Conversely, when SoF_y is small, the spatial variability of the soil properties is higher, thus requiring more GCFs for accurate modeling. As shown in Fig. 9(a), when SoF_y is large, the first few GCFs have greater importance to the model. Overall, for the *xy* plane, choosing at least 10 GCFs as input features for the subsurface model is a reasonable choice. Increasing the number of GCFs helps to capture high-frequency information. In practical cases, the number of GCFs in the *xy* plane can be treated as a hyperparameter and optimized using cross-validation methods.

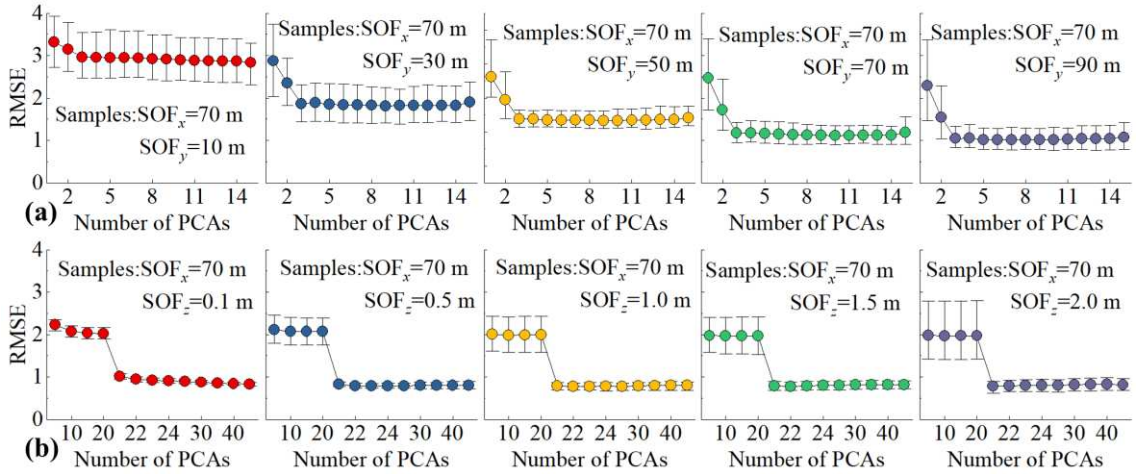

Fig.8 The impact of retaining different numbers of GCFs (number of PCAs) on the modeling accuracy in the *xy* and *xz* planes.

As shown in Fig. 8(b), in the *xz* plane, the accuracy of subsurface modeling is low when the number of GCFs is fewer than 21. However, once the 21st GCF is incorporated into the modeling process, there is a significant improvement in model accuracy. As illustrated in Fig. 4(b), the first 20 GCFs in the *xz* plane only describe the vertical correlation of the site, while the 21st GCF captures the horizontal correlation. The inclusion of the 21st GCF in subsurface modeling enhances accuracy significantly due to the combined effects of both horizontal and vertical correlations. As shown in Fig. 9(b), the 21st GCF plays a significant role in the subsurface modeling results, confirming the validity of the previous analysis. Overall, for the *xz* plane, selecting at least 25 GCFs as input parameters for

the subsurface model is a reasonable choice. In practical applications, the number of GCFs in the *xz* plane should also be optimized using cross-validation methods.

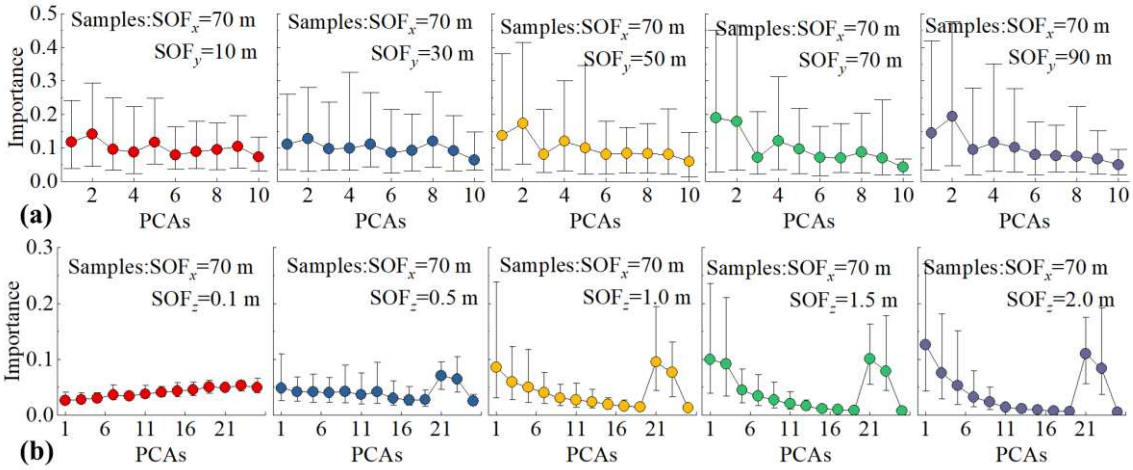

Fig.9 The importance of different GCFs on the modeling results in the *xy* and *xz* planes.

(3) ACFs Type and Its Impact on Modeling Accuracy

As shown in Figs. 10(a) and (b), the impact of different ACF types on the accuracy of subsurface modeling in the *xy* and *xz* planes is compared. The primary distinction among the ACFs lies in the roughness of the synthetic sample paths. To avoid redundancy, only 500 synthetic cases with SoF_x of 50 m are presented. In these cases, the SoF_x and SoF_y used to generate GCFs are both set at 100 m, while the SoF_z is set at 0.5 m. Statistical results indicate that the impact of different ACFs on modeling accuracy is negligible. Theoretically, when the number of GCFs actively participating in subsurface modeling is sufficiently large, the results should reflect the characteristics of the different ACFs. However, as shown in Figs. 8(a) and (b), even with an increased number of GCFs participating in subsurface modeling, the accuracy does not continuously improve. This is primarily due to the fact that the number of measured soil cells during the modeling process is significantly lower than that of the unmeasured cells. Therefore, even if more GCFs are included as input features, the model cannot learn the relationships between higher-order GCFs and soil cell properties from sparse data, leading to

the inevitable ignoring of higher-order GCFs by the model. Consequently, discussing the impact of ACF types on subsurface modeling results is only necessary when sufficient measurement data is available. However, in engineering practice, it is often not feasible to obtain copious measurement data, making the influence of different ACF types on subsurface modeling results negligible.

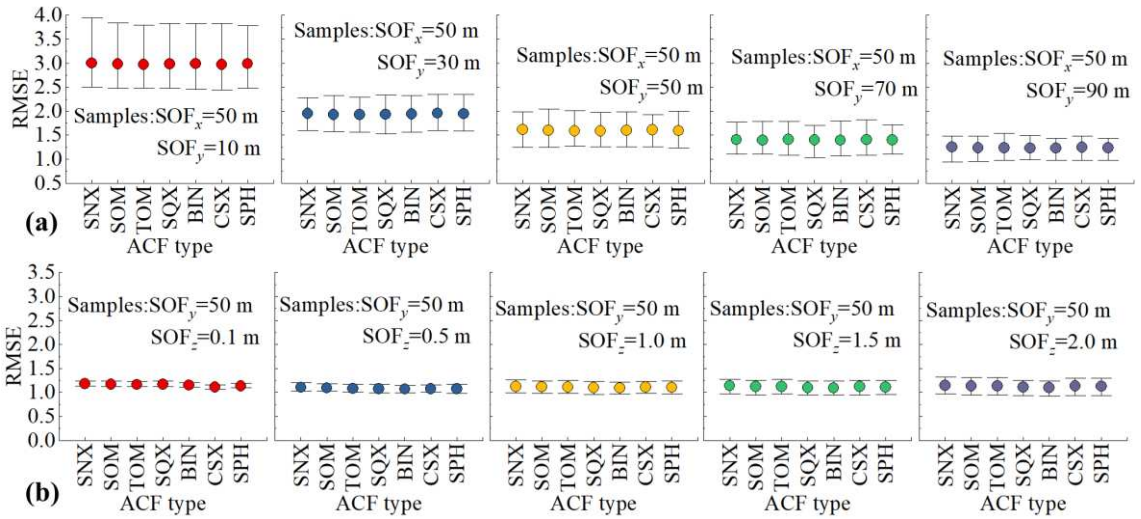

Fig.10 The impact of using different types of ACFs on the subsurface modeling results in the *xy* and *xz* planes.

4 Implementation Procedures

A Python script has been developed to perform the subsurface modeling process based on GCFs. For detailed code, please refer to https://github.com/Data-Driven-RFT/Sparse-Learning. The proposed workflow is illustrated in Fig. 11, with the key steps summarized as follows:

(1) Data collection. Collect survey data, including locations and measurement data (q). Based on the site conditions, set reasonable resolution parameters and discretize the 3D site into N soil cells.

(2) Define the range of GCFs hyperparameters. For SoF_x and SoF_y, the range is set to [x or y direction resolution, site x or y direction length]. For SoF_z, it is set to the z direction resolution. For the xy plane, the initial GCFs dimension should range between [10, 100]. For the xz and yz planes, the initial GCFs dimension should range between [25, 300].

(3) Sparse sampling to generate GCFs. The corresponding GCFs are calculated according to Eqs. (3)-(5) and then combined. It is important to note that the sampling intervals in the x and y directions should be less than or equal to $0.1 \times \mathrm{SoF}_{x/y}$, and in the z direction, the sampling interval should be less than or equal to $0.6 \times \mathrm{SoF}_{z}$. If the sampling interval is smaller than the resolution in the corresponding direction, sparse sampling is not performed.

(4) Optimize the hyperparameters for GCFs. Pair the GCFs (input features) with the corresponding soil properties (output) for the n measured soil cells, and organize them as training samples. Use cross-validation strategies to train the data-driven model and optimize the best hyperparameters for GCFs. It is important to select smaller GCFs dimensions that ensure modeling accuracy while accelerating modeling efficiency.

(5) Optimize the hyperparameters of the ML model. Use grid search to optimize the hyperparameters of the chosen machine learning model. Based on extensive synthetic case studies, it was found that for the SCNN model, the main adjustments involve the number of neural network layers and the number of neurons in each layer. For the ET model, the main adjustment involves the number of trees, while other parameters remain default. Detailed configuration and description of the SCNN and ET models can be found in Appendix B.

(6) Subsurface modeling. Use all measurement samples to train the machine learning model with the best hyperparameters. Once the model is trained, it can directly be applied to predict the properties of all soil cells across the entire site.

(7) Uncertainty estimation. Based on Eqs. (6)-(8), estimate the uncertainty in the subsurface modeling.

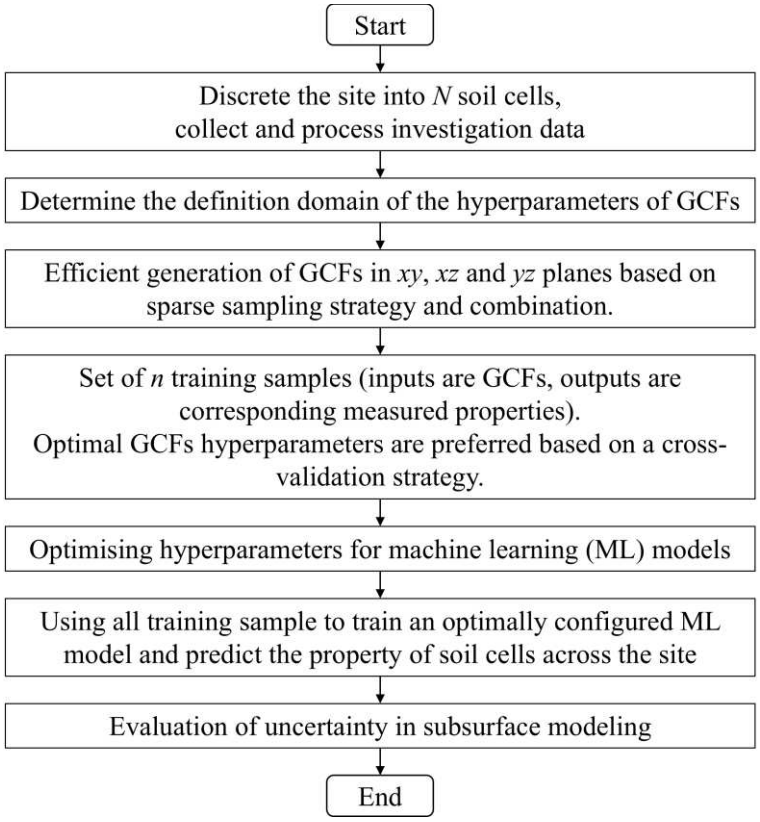

Fig.11 Process flow of the proposed subsurface modeling method based on GCFs.

5 Illustrative Example

To validate the performance of the proposed method, the model is tested on a large number of 2D stationary and nonstationary synthetic cases and compared with the alternative BCS and Kriging methods. Subsequently, the proposed method is applied to a set of 3D synthetic cases to verify its applicability for 3D sites. The BCS method is implemented using ASSD-BCS v1.2 SoFtware, which features a user-friendly visual interface (Lyu et al., 2023). The Kriging method is implemented using the Python-based Gstools v1.5.0 (Müller et al., 2022).

5.1 Comparison with SOTA Methods for 2D Stationary Cases

From the 3D synthetic samples generated in Section 3, 50 *xy* and *xz* cross-sections with different combinations of SoFs are extracted. Specifically, in the *xy* plane, the SoFs in both the *x* and *y* directions are 50 m, while in the *xz* plane, the SoFs in the *x* and *y* directions are 70 m and 1.5 m, respectively. In

522 the *xy* plane, 25 measurement points are arranged at grid points corresponding to *x* and *y* coordinates
523 of 0.5 m, 25.5 m, 50.5 m, 75.5 m, and 99.5 m. In the *xz* plane, 5 boreholes are arranged along sample
524 paths corresponding to x coordinates of 0.5 m, 25.5 m, 50.5 m, 75.5 m, and 99.5 m.

525 It is worth noting that the Kriging method uses the same ACF as the synthetic samples, and the
526 model parameters are fitted using Gstools v1.5.0 based on measurement data. As shown in Figs. 12(a)
527 and (b), the prediction results from the Kriging method are smooth, approximating the average trend
528 within a local range. The Kriging method is a parametric method, and accurately estimating random
529 field parameters is crucial for its performance. However, in engineering, only sparse measurement
530 results are often available, making it difficult to accurately estimate random field parameters, which
531 can limit the performance of the Kriging method. In contrast, both the BCS method and the proposed
532 method do not require additional parameters and exhibit good performance, as they can also estimate
533 the spatial variability of soil properties smoothly. As shown in the third case of Fig. 12(a), the proposed
534 method accurately estimates soil connectivity, which is important in soil stratification processes (T.
535 Zhao et al., 2023).

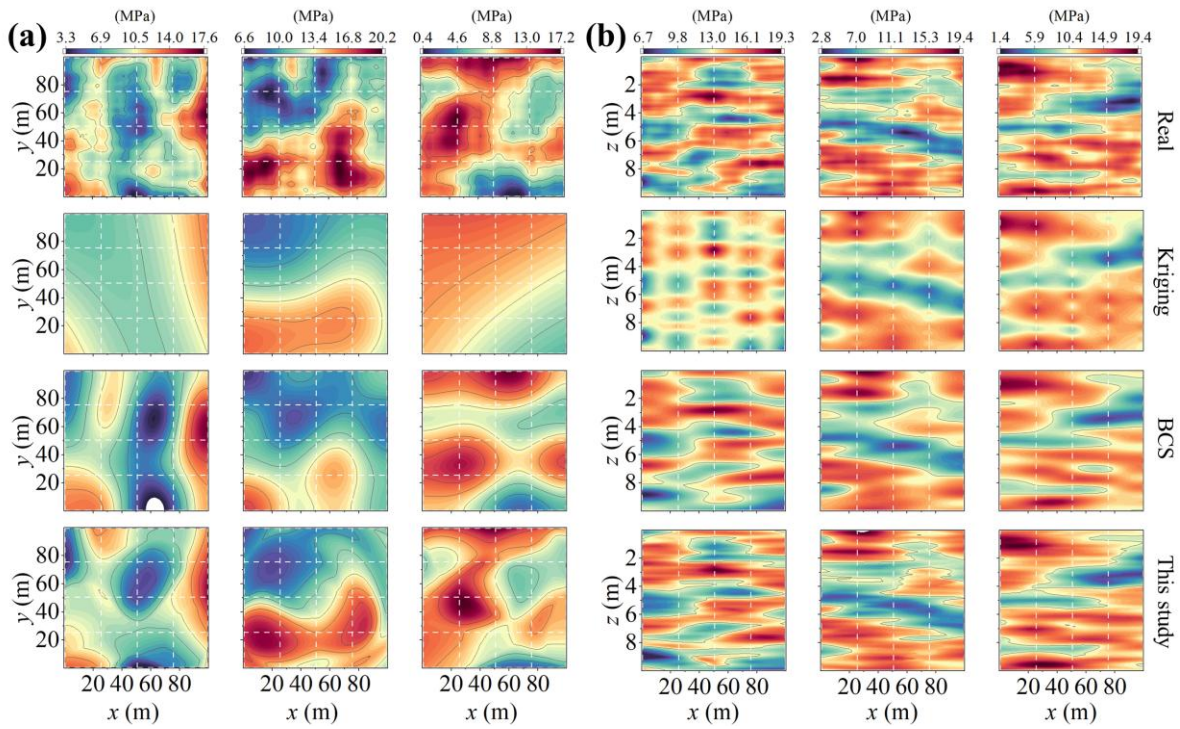

Fig. 12 Comparison of the proposed method's subsurface modeling performance with SOTA methods: (a) Comparison of three synthetic cases in the *xy* plane with SoFs of 50 m in both *x* and *y* directions; (b) Comparison of three synthetic cases in the *xz* plane with SoFs of 70 m and 1.5 m in the *x* and *z* directions, respectively.

As shown in Fig. 13, the performance of the Kriging, BCS, and the proposed methods is summarized. In the *xy* plane, the evaluation metrics of the Kriging and BCS methods are close, with both capturing the average trend of the field. The proposed method achieves an average R^2 greater than 0.5, and *RMSE* and *sMAPE* less than 2 and 15%, respectively, outperforming both Kriging and BCS. In the *xz* plane, the R^2 values of the BCS and proposed methods are greater than those of the Kriging method, and their *RMSE* and *sMAPE* are lower. This indicates the BCS and the proposed methods have significant advantages when more sample points are known. Moreover, the proposed method achieves an R^2 close to 1, and *RMSE* and *sMAPE* less than 1 and 7%, respectively, further validating its superior performance.

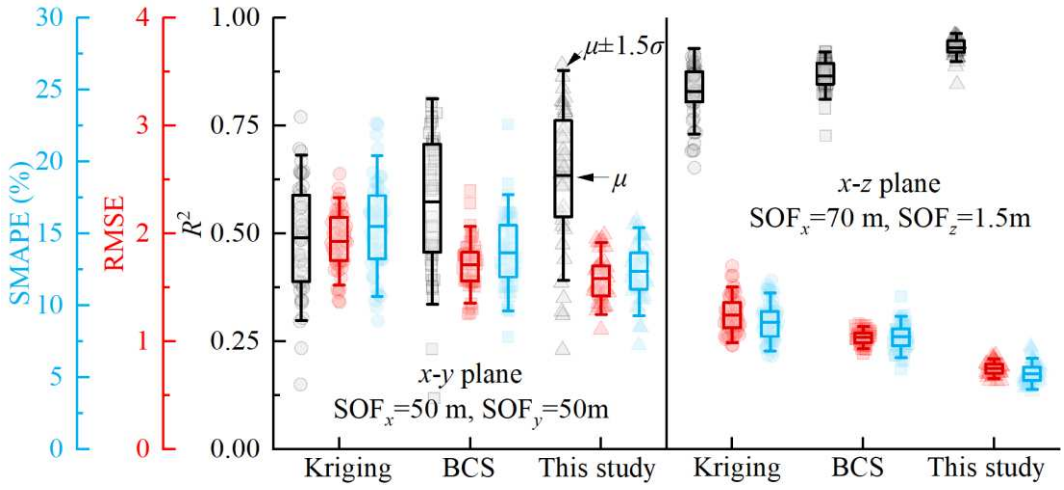

Fig. 13 Statistical analysis of R^2, *RMSE*, and *sMAPE* for different modeling methods.

As shown in Figs. 14(a) and (c), the model uncertainty for the first case in Figs. 12(a) and (b) is displayed. The uncertainty of the proposed method is characterized by the standard deviation of the prediction results from 50 randomly initialized SCNN models, and the detailed calculation process is provided in Section 2.3. It can be observed that the model uncertainty is zero at the measurement locations, and the uncertainty increases as the distance from the measurement location grows. Additionally, the model uncertainty is also related to the spatial variability of the surrounding soil properties. Moreover, the uncertainty in the *xy* plane is significantly higher than in the *xz* plane, indicating that an increase in measurement data can substantially reduce the model uncertainty. As shown in Figs. 14(b) and (d), the model uncertainty of the proposed method is compared with that of the BCS method. The BCS method shows high uncertainty at the measurement locations because the predictions from the BCS method do not match the measured data exactly at the measurement locations, which clearly contradicts the reality. Overall, the uncertainty range of the proposed method is in close agreement with the BCS method, validating the effectiveness of the proposed approach.

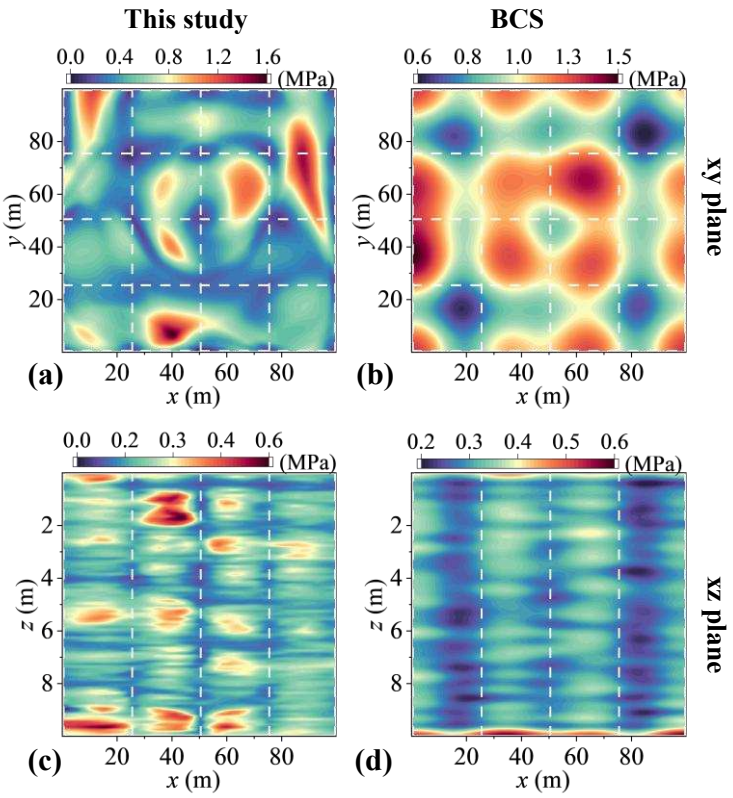

Fig. 14 Comparison of modeling uncertainty (standard deviation) between the proposed method and the BCS method in the (a) & (b) *xy* plane, (c) & (d) *xz* plane.

5.2 Comparison with BCS Method for 2D Nonstationary Cases

To more comprehensively validate the performance of the proposed method, trend terms are introduced into the 100 stationary random fields used in Section 5.1. A random linear trend $\alpha \times x$(or y) is assumed in the x and y directions, where the random coefficient α ranges from 0.02 to 0.05. Similarly, a random linear trend $\beta \times z$ is assumed in the z direction, with the random coefficient β ranging from 0.2 to 0.5. This section primarily evaluates the ability of the proposed method to perform subsurface modeling directly based on non-stationary data. This approach helps reduce the uncertainty caused by manual detrending and enhances the efficiency of automated modeling. Since Kriging requires additional detrending when applied to non-stationary random fields, only the proposed method and the BCS method are compared here. As shown in Fig. 15, the R^2 values of BCS and the proposed method

fluctuate between 0.4 and 0.85 in the *xy*-plane. This variation is primarily due to the limited number of known data points (25 points), which account for only 0.25% of the total soil cells. In the *xz*-plane, where the number of known data points increases significantly (500 points), both BCS and the proposed method perform well, with R^2 values exceeding 0.8. However, the proposed method demonstrates more consistent performance, with smaller fluctuations in R^2, *RMSE*, and *SMAPE* compared to the BCS method. This indicates that the proposed method improves modeling accuracy and is suitable for both stationary and non-stationary data with mild trends.

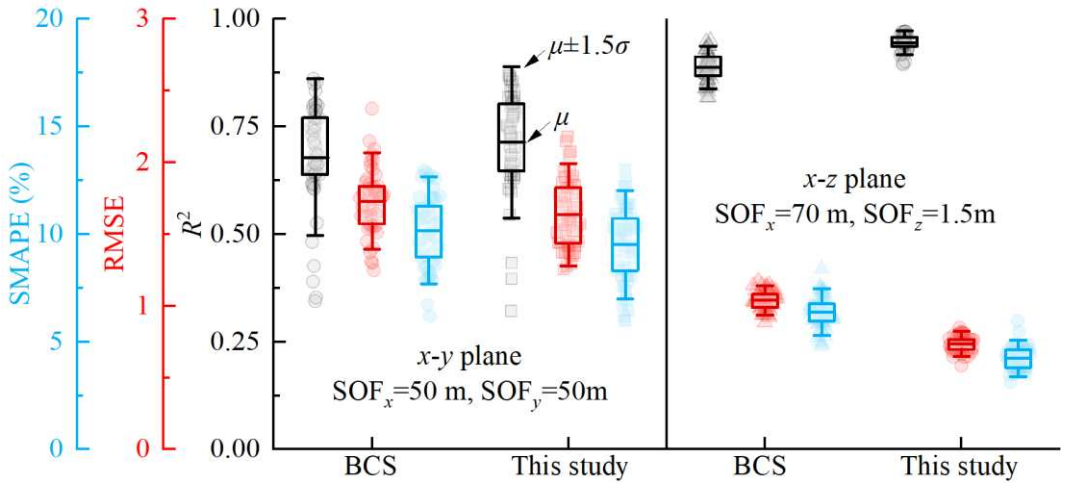

Fig. 15 Performance comparison between the BCS method and the proposed method in nonstationary cases.

5.3 Performance of the Proposed Method for 3D Cases

Three 3D cases are extracted from the synthetic random field samples in Section 3 to validate the proposed method: Case #1 (SoF_x: 50 m, SoF_y: 50 m, SoF_z: 1 m), Case #2 (SoF_x: 90 m, SoF_y: 50 m, SoF_z: 0.5 m), and Case #3 (SoF_x: 90 m, SoF_y: 50 m, SoF_z: 1 m), as illustrated in Figs. 16(a), (e), and (i). For each synthetic site, the measurement points are established at grid points corresponding to *x* and *y* values of 0.5 m, 25.5 m, 50.5 m, 75.5 m, and 99.5 m, resulting in a total of 25 sample paths used as training data.

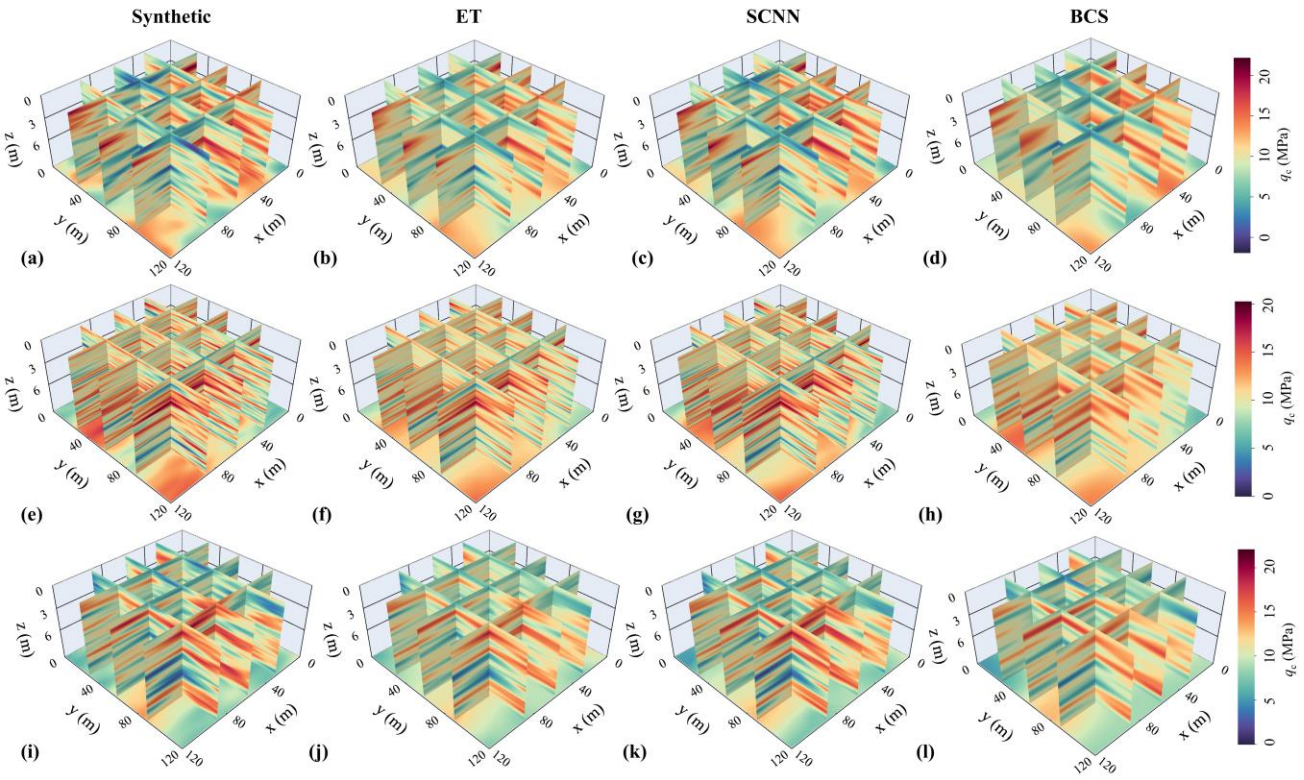

Fig.16 Performance of the proposed method in synthetic 3D cases: (a)-(d) show the synthetic site for Case #1, along with the modeling results using ET, SCNN and BCS; (e)-(h) present the modeling results for Case #2; (i)-(l) depict the modeling results for Case #3.

It is important to note that the framework proposed is flexible, meaning that after generating the GCFs, various machine learning models can be employed for subsurface modeling. The primary subsurface modeling approach employed in this study is the SCNN model. To conduct a more comprehensive comparison, the ET approach is used due to its strong fitting capabilities. Figs. 16(a) to (d) illustrate the true distribution of soil properties for synthetic Case #1, the results obtained using ET, SCNN, and BCS modeling, respectively. Figs. 16(e) to (h) and Figs. 16(i) to (l) present the prediction results for Case #2 and Case #3, respectively. It is observed that using the proposed method yields subsurface modeling results consistent with the true distribution, regardless of whether ET or SCNN is used. However, the results obtained from ET and BCS modeling tend to approximate the

average more closely. In contrast, the results from SCNN modeling align more closely with the true distribution. As shown in Table 1, the predictive results of the SCNN model demonstrate a higher R^2 compared to the ET and BCS models, further validating the superiority of the SCNN approach. The *RMSE* and *MAPE* values for the ET and SCNN models are relatively similar. Therefore, averaging the predictive results of the ET and SCNN models reveals that while the R^2 of the average model decreases relative to the SCNN model, the *RMSE* and *MAPE* for the average model achieve lower values in Case #1 and Case #2. Thus, adopting the average model may be a more robust choice, especially when faced with sparse known information, as stacking multiple algorithms often enhances the model's reliability. Furthermore, both the ET and SCNN models take only 2-3 minutes for modeling and prediction, with the ET model being slightly faster than the SCNN model. Therefore, for engineering applications, it is acceptable to integrate multiple algorithms for subsurface modeling to obtain more robust prediction results.

Table 1 Comparison of subsurface modeling performance of different models in 3D synthetic cases

	Model	R^2	RMSE (MPa)	MAPE (%)
Case #1 (SoFx=50, SoFy=50, SoFz=1)	BCS	0.571	1.903	17.437
	ET	0.499	1.745	14.513
	SCNN	**0.750**	1.598	14.909
	Mean	0.683	**1.576**	**13.574**
Case #2 (SoFx=90, SoFy=50, SoFz=0.5)	BCS	0.489	1.937	15.133
	ET	0.545	1.350	10.249
	SCNN	**0.730**	1.350	10.769
	Mean	0.689	**1.267**	**9.738**
Case #3 (SoFx=90, SoFy=50, SoFz=1)	BCS	0.473	1.742	17.797
	ET	0.445	1.573	11.975
	SCNN	**0.772**	**1.344**	**10.469**
	Mean	0.682	1.373	10.507

Note: 'Mean' refers to the average of the prediction results from the ET and SCNN models.

6 Real Data Case Study

6.1 Baytown, TX, USA

As shown in Fig. 17, the rectangular test site is located in the eastern region of the intersection of Interstate-10 and Route-146 in Baytown, Texas (Stuedlein, 2008). Baytown is situated to the north of Upper Galveston Bay, which is part of the San Jacinto River, with the San Jacinto River flowing south into Galveston Bay and north into Lake Houston. The test site is located in the Quaternary coastal plain of Texas, which forms a band-shaped zone about 110-150 km wide, parallel to the Gulf of Mexico coastline (Stuedlein et al., 2012a). The soil at the test site consists of the Beaumont Clay Layer, which is composed of brownish-red and brownish-gray clay, occasionally interspersed with fine sand and silt layers. The Beaumont Clay Layer was deposited in the floodplains at the beginning of the Wisconsin glacial period. Additionally, the terrace has been influenced by the long-term lowering of the Gulf of Mexico during the post-depositional glacial period, causing global preconsolidation (O'Neill, 2014). As the Beaumont Clay Layer dried, it developed a series of slickensides, fissures, and a few joints.

A series of in-situ tests, including the standard penetration test (SPT), thin-walled tube sampling, and cone penetration test (CPTu), were conducted at the test site to characterize the subsurface conditions (Stuedlein et al., 2012a). As shown in Fig. 18, this study focuses on the results from 9 sets of CPTu tests, using the cone tip resistance measurements as an example for subsurface modeling. According to the survey results, the test site was divided into four different soil layers. The very stiff desiccated clay crust extends to an average depth of about 0.66 m from the surface. The second layer, the upper clay layer, extends to an average depth of 3.74 m and consists of medium stiff lean clay. Notably, CPT-3 reveals a 1-meter-thick soft zone at a depth of 1.66 m. Samples recovered from the

upper clay layer typically contain many cracks and occasional slickensides. The third layer consists of loose silty sand/sandy silt (SM/ML), extending from an average depth of 3.74 to 4.5 m. Below 4.5 m, the lower clay layer is present, consisting of stiff, slightly silty, and fat clay (CH) (Stuedlein et al., 2012b, 2012a). CPTu data can be directly downloaded from the ISSMGE TC304 database (http://140.112.12.21/issmge/tc304.htm).

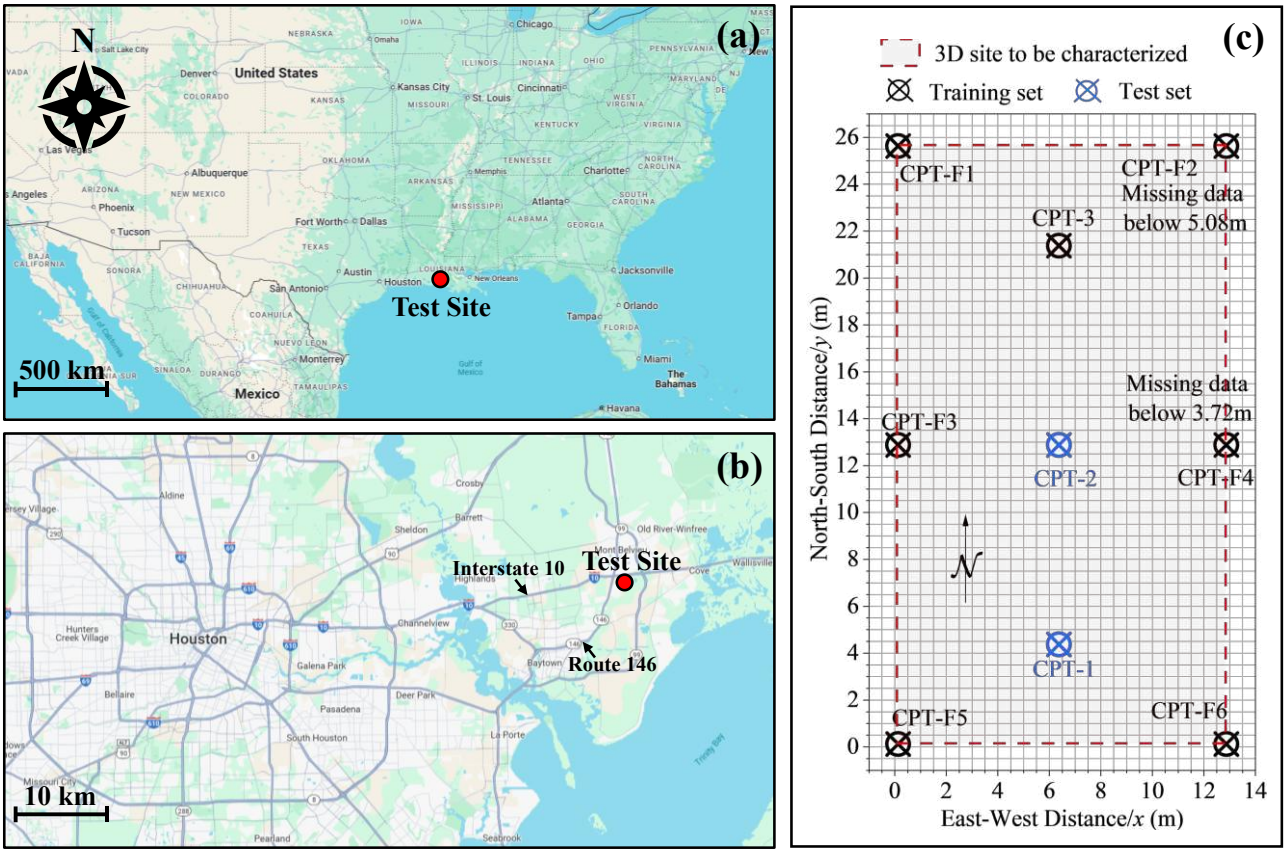

Fig. 17 Geographical layout of the test site in Baytown, Texas, USA: (a) The location of the test site in Texas, USA; (b) The location of samples in Baytown; (c) The distribution of the collocated borehole and CPTs. Map data from Google Earth.

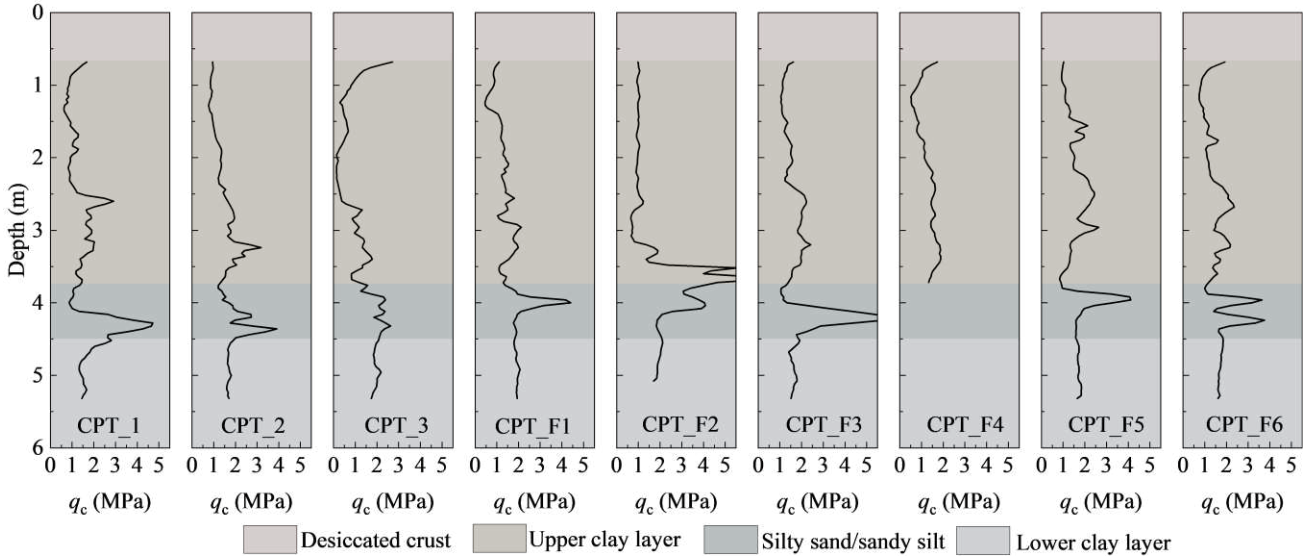

Fig. 18 Nine CPT measurements and the average stratigraphy of the site (raw data can be accessed from http://140.112.12.21/issmge/tc304.htm).

The test site has a length of 13 m in the x (east-west) direction and 26 m in the y (north-south) direction. In the z direction, the focus is mainly on the clay layer and silty sand/sandy silt layer at depths between 0.68 m and 5.32 m, consistent with Stuedlein et al. (2012a). The resolution is set at 0.25 m in both the x and y directions, and 0.04 m in the z direction. As shown in Fig. 17, a total of 7 sets of measurements, including CPT_3 and CPT_F1-F6, are used to construct the subsurface model, while the remaining data from CPT-1 and CPT-2 are used for model validation. As shown in Fig. 18, some of the measurement paths are incomplete. For example, CPT_F2 is missing data below a depth of 5.08 m, and CPT_F4 is missing data below a depth of 3.72 m. In engineering practice, measurement data often have missing sections due to limitations in equipment, operation, and site conditions. It is worth noting that the proposed method does not require complete measurement data, making it widely applicable to situations with missing data.

As shown in Fig. 19, the subsurface modeling results and their uncertainty based on the SCNN model are presented. For detailed configuration of the SCNN model and the subsurface modeling code,

please refer to Appendix B. Fig. 19(a) shows the average of the subsurface modeling results from 50 SCNN models with different initialized trainable parameters, while Fig. 19(b) shows the standard deviation of the 50 modeling results. It can be observed that there is a thin interlayer at a depth of 4 m, which perfectly aligns with the field exploration results (SM/ML is distributed within the 3.74–4.5 m depth range). Furthermore, the model exhibits small uncertainty at the locations of the training samples. Since CPT_2 and CPT_1 are not involved in the training process, there is higher uncertainty at their respective locations. Additionally, compared to CPT_2, the location of CPT_1 is farther from the training samples, resulting in greater uncertainty in the model's prediction of the CPT_1 sample path.

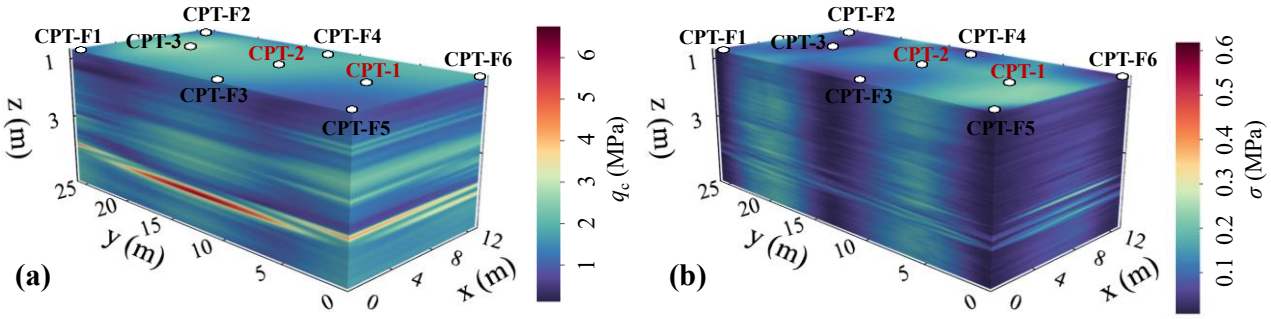

Fig. 19 Subsurface modeling results of the proposed method in the Baytown, TX, USA case: (a) Subsurface modeling results based on 6 CPT measurement data; (b) Uncertainty of subsurface modeling results.

As shown in Fig. 20, model prediction performance and uncertainty on the test set are presented. Due to missing sample paths in CPT_F2 and CPT_F4, these missing positions are excluded from the model training and considered as part of the test set. In the upper parts of CPT_F2 and CPT_F4 (training data), the model's predictions exactly match the measured data, indicating that the model has successfully learned the high-dimensional nonlinear mapping between GCFs (input features) and corresponding q_c (output) at these positions. Furthermore, the model shows good agreement with the measured data at the CPT_1 and CPT_2 positions, with most of the measurement data included within

687 the 95% confidence interval. Additionally, the model successfully predicted the presence of the silty
688 sand/sandy silt layer below 3.72m in CPT_F4.

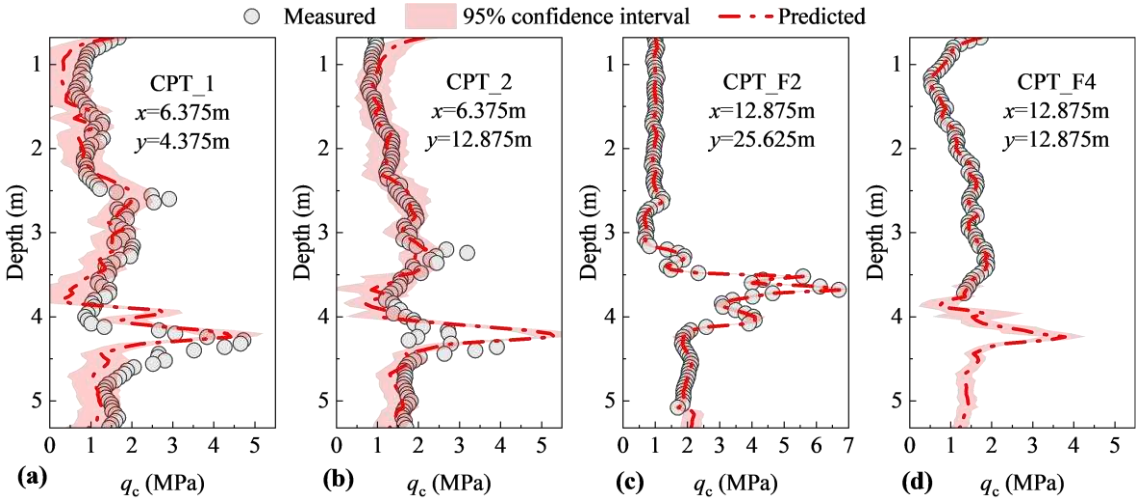

689

690 Fig.20 Prediction results and uncertainty of the proposed method at test locations.

691 **6.2 Christchurch, New Zealand**

692 As shown in Fig. 21, the test site is located in Christchurch, New Zealand, where 34 sets of CPT
693 data are collected from a 120 m × 120 m square site. The measurement data can be accessed directly
694 from the New Zealand Geotechnical Database (NZGD) (NZGD, 2023). According to the Robertson
695 method (Robertson, 1990; Robertson and Wride, 1998) for soil classification, the soil behavior type
696 index (I_c) generally ranges from 1.1 to 2.6. The surface layer is primarily composed of dense sand to
697 gravelly sand, while the layer beneath is mainly clean sand to silty sand, occasionally interspersed with
698 silty sand to sandy silt. It is important to note that there are significant data gaps near the surface in the
699 34 CPT measurements. To better validate the proposed method, test data from depths of 5-15m below
700 the surface are collected for subsurface modeling. The site resolution is set at 1 m in both the x and y
701 directions, and 0.1 m in the z direction.

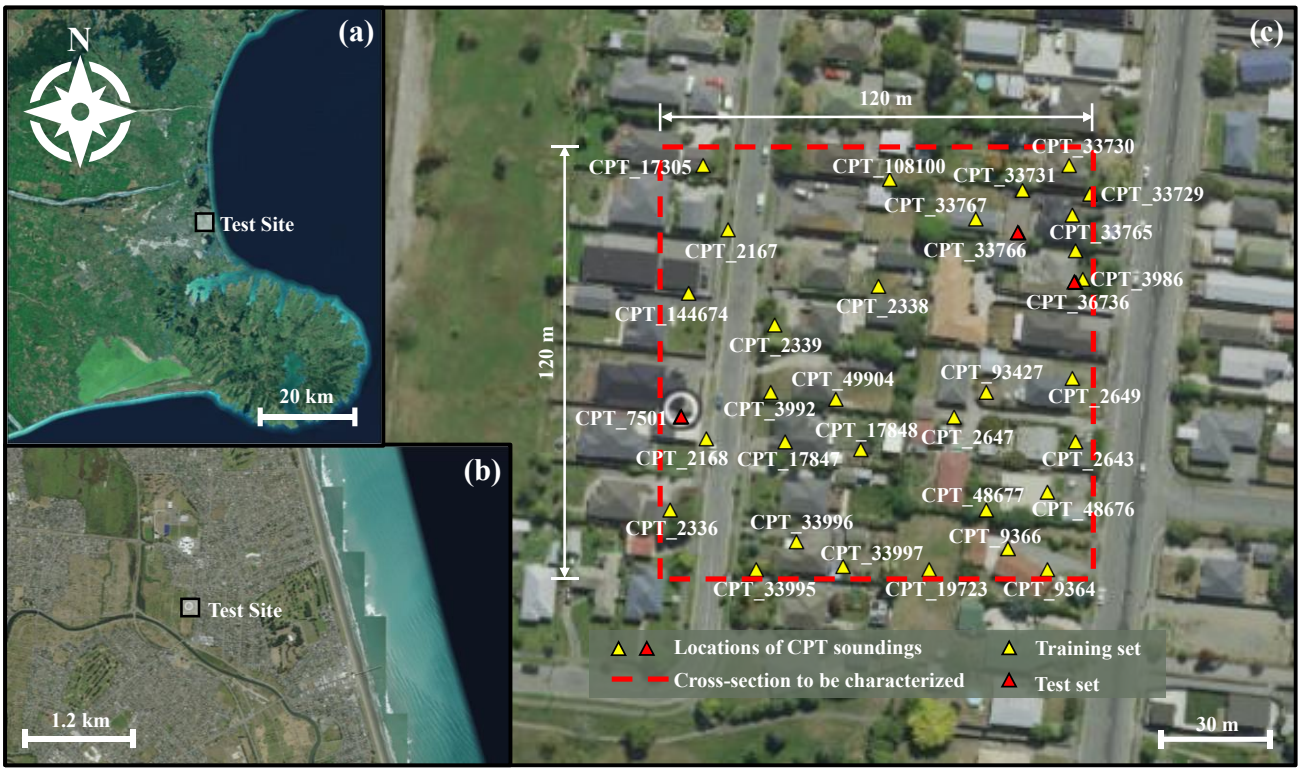

Fig.21 Geographical layout of 34 CPT surveys in Christchurch, New Zealand: (a) The location of the test site in New Zealand; (b) The location of samples in Christchurch; (c) The distribution of the collocated CPTs. (Note: CPT codes used are consistent with the New Zealand Geotechnical Database)(NZGD, 2023).

Fig. 22(a) shows the CPT sample paths used for subsurface modeling in the Christchurch case, where some sample paths are incomplete. It is noteworthy that the proposed method does not require complete data at sampling locations, allowing it to be applied with more flexibility in practice. CPT_7501, CPT_33766, and CPT_36736 are reserved for the model testing, while the remaining 31 CPT soundings are used for model training. Fig. 22(b) presents the average subsurface modeling results of the SCNN and ET models, where the q_c values are generally low at depths above 3 m and increase with depth in the 3-10 m range, indicating the trend in soil distribution. Figs. 23(a)-(c) show the predicted results of the model at the three test locations: CPT_7501, CPT_33766, and CPT_36736, along with their 95% confidence intervals. It can be observed that the predicted sample paths align

well with the measured data, with most test data falling within the 95% confidence interval. Additionally, the model exhibits greater uncertainty at CPT_7501 and CPT_33766 due to the limited number of boreholes in their vicinity. In contrast, the location of CPT_36736 is in close proximity to CPT_3986 used for subsurface modeling, resulting in lower uncertainty at this position. This further validates the rationale behind the proposed method for assessing subsurface modeling uncertainty.

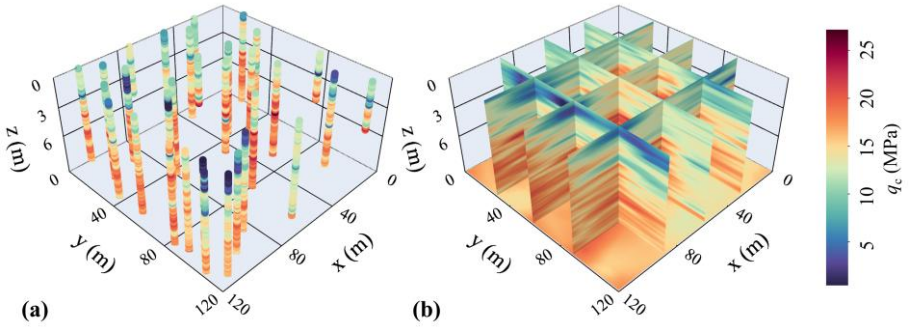

Fig.22 Performance of the proposed method in real 3D cases: (a) represents the measured CPT sample paths from the New Zealand case; (b) shows the average modeling results of ET and SCNN based on 31 training data.

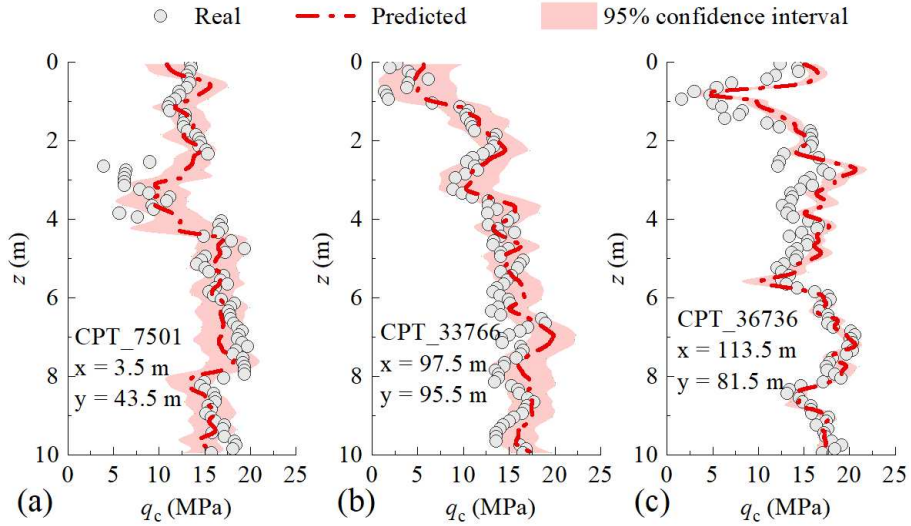

Fig.23 The subsurface modeling results and uncertainties at three test locations.

7 Conclusions

This study proposes an enhanced data-driven framework that uses random field theory to recover subsurface geotechnical properties in the presence of sparse in-situ test data. Additionally, statistical

730 analyses are conducted to reduce the computational complexity of the proposed method and eliminate
731 additional parameters. Finally, the superiority of the proposed method is validated through a series of
732 synthetic cases and two real cases. Based on the findings, the following conclusions can be drawn:
733 (1) The proposed subsurface modeling framework is capable of integrating random field theory
734 into data-driven models through geotechnical correlation fields, providing a variety of basis functions
735 for subsurface modeling. Validation through 2D and 3D synthetic cases, as well as two real cases,
736 shows that the method generally exhibits higher R^2 and lower *RMSE* and *MAPE* compared to the
737 alternative Kriging and BCS methods.
738 (2) The strategy of first performing sparse sampling and then projecting into the principal
739 component space effectively reduces the computational complexity of PCA operations in the process
740 of obtaining GCFs. This approach also avoids the challenges associated with storing and processing
741 large correlation matrices for large or high-resolution sites.
742 (3) The influence of random field parameters (SoF and ACF) on subsurface modeling results is
743 investigated. Since geotechnical measurement data are generally sparse in the horizontal direction and
744 denser in the vertical direction, using larger horizontal SoF (greater than 2 times the borehole spacing)
745 and smaller vertical SoF (site vertical resolution) to generate GCFs can significantly improve modeling
746 accuracy. Additionally, in cases of sparse measurement data, the type of ACFs has a negligible
747 influence on the modeling results.
748 (4) The framework proposed is flexible, allowing for the application of different machine learning
749 models for subsurface modeling after generating GCFs. Validation against a series of 3D sites revealed
750 that the modeling results of the proposed SCNN model exhibit a higher R^2 compared to an extreme

random tree model. Furthermore, the average predictions from both the extreme random tree and shortcut-connected neural network models demonstrated lower *RMSE* and *MAPE*. Therefore, it is recommended to employ a stacking strategy using multiple algorithms to enhance the robustness of underground modeling.

It should be noted that when subsurface conditions involve weak interlayers or soil layers with significant differences in properties, the spatial distribution of the subsurface stratigraphic boundaries can be predefined. Then, the proposed method can be used to model the spatial variability of soil properties within each layer. Additionally, measurement data for weak interlayers often constitute only a small portion of the total data, leading to potential prediction errors due to data imbalance. Further exploration of improvement strategies for data-driven subsurface modeling methods under conditions of data imbalance is needed.

CRediT authorship contribution statement

Weihang Chen: Conceptualization, Investigation, Data curation, Methodology, SoFtware, Validation, Writing – original draft, Writing – review & editing, Funding acquisition. **Chao Shi:** Conceptualization, Investigation, Writing – review & editing. **Jianwen Ding:** Conceptualization, Funding acquisition, Supervision, Writing – review & editing. **Tengfei Wang:** Conceptualization, Investigation, Writing – review & editing. **David P. Connolly:** Conceptualization, Investigation, Writing – review & editing.

Acknowledgments

This study was supported by the National Natural Science Foundation of China (Grant No. 52378330), the Natural Science Foundation of Sichuan Province (Grant No. 2023NSFSC0391), the 111 Project (Grant No. B21011), the Postgraduate Research & Practice Innovation Program of Jiangsu

Province (Grant No. SJCX23_0084), and the SEU Innovation Capability Enhancement Plan for Doctoral Students (Grant No. CXJH_SEU 24182).

Appendix A.

Table A1. Frequently Used Autocorrelation Functions (ACFs) - Adapted from Cami et al. (2020)

Model	Autocorrelation function $\rho_{i,j}$	Frequency of usage
Single exponential (SNX)	$\exp\left[-2\left(\frac{\lvert\tau_{i,j}^{x}\rvert}{SOF_x}+\frac{\lvert\tau_{i,j}^{y}\rvert}{SOF_y}\right)\right]$	47 %
Spherical (SPH)	$\begin{cases}\left[1-\frac{9}{8}\frac{\lvert\tau_{i,j}^{x}\rvert}{SOF_x}+\frac{27}{128}\left(\frac{\lvert\tau_{i,j}^{x}\rvert}{SOF_x}\right)^3\right]\left[1-\frac{9}{8}\frac{\lvert\tau_{i,j}^{y}\rvert}{SOF_y}+\frac{27}{128}\left(\frac{\lvert\tau_{i,j}^{y}\rvert}{SOF_y}\right)^3\right] & \lvert\tau_{i,j}^{x}\rvert\le\frac{4}{3}SOF_x \text{ and } \lvert\tau_{i,j}^{y}\rvert\le\frac{4}{3}SOF_y \\ 0 & \text{otherwise}\end{cases}$	15 %
Squared exponential (SQX)	$\exp\left[-\pi\left(\frac{{\tau_{i,j}^{x}}^2}{SOF_x^2}+\frac{{\tau_{i,j}^{y}}^2}{SOF_y^2}\right)\right]$	15 %
Cosine exponential (CSX)	$\cos\left(\frac{\lvert\tau_{i,j}^{x}\rvert}{SOF_x}\right)\cos\left(\frac{\lvert\tau_{i,j}^{y}\rvert}{SOF_y}\right)\exp\left(-\left(\frac{\lvert\tau_{i,j}^{x}\rvert}{SOF_x}+\frac{\lvert\tau_{i,j}^{y}\rvert}{SOF_y}\right)\right)$	10 %
Binary noise (BIN)	$\begin{cases}\left(1-\frac{\lvert\tau_{i,j}^{x}\rvert}{SOF_x}\right)\left(1-\frac{\lvert\tau_{i,j}^{y}\rvert}{SOF_y}\right) & \lvert\tau_x\rvert\le SOF_x \text{ and } \lvert\tau_y\rvert\le SOF_y \\ 0 & \text{otherwise}\end{cases}$	9 %
Second–order Markov (SOM)	$\left(1+4\frac{\lvert\tau_{i,j}^{x}\rvert}{SOF_x}\right)\left(1+4\frac{\lvert\tau_{i,j}^{y}\rvert}{SOF_y}\right)\exp\left[-4\left(\frac{\lvert\tau_{i,j}^{x}\rvert}{SOF_x}+\frac{\lvert\tau_{i,j}^{y}\rvert}{SOF_y}\right)\right]$	4 %
Third–order Markov (TOM)	$\left(1+\frac{16}{3}\frac{\lvert\tau_{i,j}^{x}\rvert}{SOF_x}+\frac{256}{27}\left(\frac{\lvert\tau_{i,j}^{x}\rvert}{SOF_x}\right)^2\right)\left(1+\frac{16}{3}\frac{\lvert\tau_{i,j}^{y}\rvert}{SOF_y}+\frac{256}{27}\left(\frac{\lvert\tau_{i,j}^{y}\rvert}{SOF_y}\right)^2\right)\exp\left(-\frac{16}{3}\left(\frac{\lvert\tau_{i,j}^{x}\rvert}{SOF_x}+\frac{\lvert\tau_{i,j}^{y}\rvert}{SOF_y}\right)\right)$	New

Note: $\rho_{i,j}$ represents the correlation between soil cells i and j. $\tau_{i,j}^{x}$ and $\tau_{i,j}^{y}$ are the spacing of soil cell i and j in the x and y directions. SOF_x and SOF_y are the scales of fluctuation in the x and y directions, respectively.

Appendix B.

The code used in this study can be found in https://github.com/Data-Driven-RFT/Sparse-Learning, which includes: ① a case for generating GCFs, and ② the complete subsurface modeling process based on the Baytown, TX, USA case.

Recently, ensemble learning algorithms with powerful nonlinear regression capabilities have been widely used in geotechnical engineering (Xie et al., 2024), such as Random Forest (RF), Extra Trees

(ET), and Gradient Boosting (GB). Both ET and RF algorithms are based on the BAGGING (Bootstrap Aggregating) ensemble technique. The RF algorithm constructs multiple subsets using random sampling with replacement, and each subset is used to build a corresponding regression tree. In contrast, the ET algorithm trains each regression tree on the entire dataset, which reduces prediction bias. Additionally, the ET algorithm introduces extra randomness in the tree-building process by randomly selecting split thresholds to compute the split points for each variable, and then selecting the best split point based on the scoring criterion to reduce prediction bias. Compared to RF, when the number of regression trees is sufficiently large, ET can generate continuous and smooth prediction results. Therefore, the ET algorithm is better suited for modeling continuous geotechnical sites or random fields. A detailed introduction to the ET algorithm can be found in Simm et al. (2014). In this study, the ET model is constructed using the Python-based Scikit-learn v1.1.3 library (Pedregosa et al., 2018).

As shown in Fig. A1, this study uses a shortcut-connected neural network model (SCNN) for subsurface modeling. The SCNN integrates input features with high-level features extracted by hidden layers, thus mitigating the risk of gradient vanishing and explosion, and improving training efficiency and model performance. The SCNN model formulation is as follows:

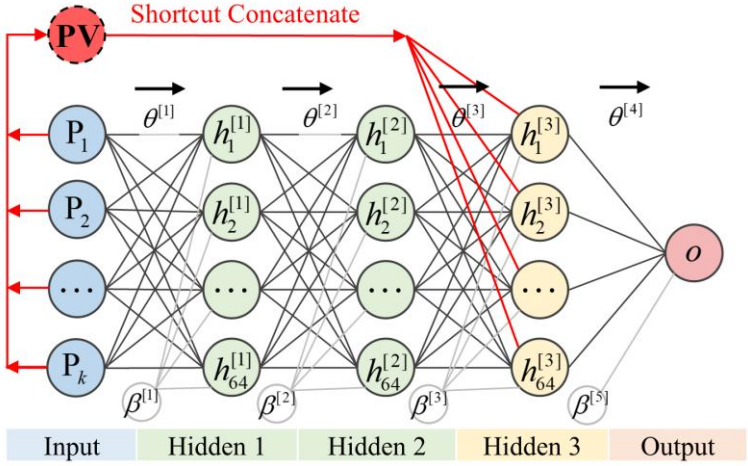

Fig. A1 The SCNN model architecture for subsurface modeling (Note: P_1 to P_k correspond to the k

principal components in the **PV** vector.)

$$\boldsymbol{h}^1 = \mathrm{ReLU}(\mathbf{PV}, \boldsymbol{\theta}^1, \boldsymbol{\beta}^1) \tag{A1}$$

$$\boldsymbol{h}^2 = \mathrm{ReLU}(\boldsymbol{h}^1, \boldsymbol{\theta}^2, \boldsymbol{\beta}^2) \tag{A2}$$

$$\boldsymbol{h}^3 = \mathrm{ReLU}(\mathrm{concatenate}(\mathbf{PV}, \boldsymbol{h}^2), \boldsymbol{\theta}^3, \boldsymbol{\beta}^3) \tag{A3}$$

$$\boldsymbol{o} = \mathrm{Linear}(\boldsymbol{h}^3, \boldsymbol{\theta}^4, \boldsymbol{\beta}^4) \tag{A4}$$

where $\boldsymbol{h}$ represents the hidden layer feature vector of the neural network. θ and β are the feature weights and bias terms for each layer, respectively, with no trainable θ and β parameters in the input layer. The concatenation operation in the third hidden layer directly combines the input feature **PV** with the feature vector $\boldsymbol{h}^2$ from the second hidden layer. The output of the model is denoted as $\boldsymbol{o}$. The model consistently uses the ReLU activation function due to its computational simplicity and rapid convergence rate (P. Zhang et al., 2022). Model training is based on the Nadam optimizer, an extension of the Adam optimizer that incorporates Nesterov momentum and RMSprop. The hyperparameters for the model are determined using grid search. The number of neurons in the hidden layers is set to 64, the learning rate is 0.001, and the number of iterations is 500. In this study, the SCNN model is constructed using the Python-based Tensorflow v2.8.0 library (Abadi et al., 2016).

References

Abadi, M., Barham, P., Chen, J., Chen, Z., Davis, A., Dean, J., Devin, M., Ghemawat, S., Irving, G., Isard, M., Kudlur, M., Levenberg, J., Monga, R., Moore, S., Murray, D.G., Steiner, B., Tucker, P., Vasudevan, V., Warden, P., Wicke, M., Yu, Y., Zheng, X., 2016. TensorFlow: a system for large-scale machine learning, in: Proceedings of the 12th USENIX Conference on Operating Systems Design and Implementation, OSDI'16. USENIX Association, USA, pp. 265–283.

Cami, B., Javankhoshdel, S., Phoon, K.-K., Ching, J., 2020. Scale of Fluctuation for Spatially Varying Soils: Estimation Methods and Values. ASCE-ASME J. Risk Uncertain. Eng. Syst. Part Civ. Eng. 6, 03120002. https://doi.org/10.1061/AJRUA6.0001083

Chen, W., Ding, J., Shi, C., Wang, T., Connolly, D.P., 2024. Geotechnical correlation field-informed and data-driven prediction of spatially varying geotechnical properties. Comput. Geotech. 171, 106407. https://doi.org/10.1016/j.compgeo.2024.106407

828 Chen, W., Ding, J., Wang, T., Connolly, D.P., Wan, X., 2023. Soil property recovery from incomplete
829 in-situ geotechnical test data using a hybrid deep generative framework. Eng. Geol. 326,
830 107332. https://doi.org/10.1016/j.enggeo.2023.107332
831 Ching, J., Phoon, K.-K., Stuedlein, A.W., Jaksa, M., 2019. Identification of sample path smoothness
832 in soil spatial variability. Struct. Saf. 81, 101870.
833 https://doi.org/10.1016/j.strusafe.2019.101870
834 Collico, S., Arroyo, M., Devincenzi, M., 2024. A simple approach to probabilistic CPTu-based
835 geotechnical stratigraphic profiling. Comput. Geotech. 165, 105905.
836 https://doi.org/10.1016/j.compgeo.2023.105905
837 Gong, W., Zhao, C., Juang, C.H., Zhang, Y., Tang, H., Lu, Y., 2021. Coupled characterization of
838 stratigraphic and geo-properties uncertainties – A conditional random field approach. Eng.
839 Geol. 294, 106348. https://doi.org/10.1016/j.enggeo.2021.106348
840 Guan, Z., Wang, Y., Cao, Z., Hong, Y., 2020. Smart sampling strategy for investigating spatial
841 distribution of subsurface shallow gas pressure in Hangzhou Bay area of China. Eng. Geol.
842 274, 105711. https://doi.org/10.1016/j.enggeo.2020.105711
843 Guan, Z., Wang, Y., Phoon, K.-K., 2024a. Data-driven geotechnical site recognition using machine
844 learning and sparse representation. Eng. Geol. 107893.
845 https://doi.org/10.1016/j.enggeo.2024.107893
846 Guan, Z., Wang, Y., Phoon, K.-K., 2024b. Dictionary Learning of Spatial Variability at a Specific Site
847 Using Data from Other Sites. J. Geotech. Geoenvironmental Eng. 150, 04024072.
848 https://doi.org/10.1061/JGGEFK.GTENG-12408
849 Hu, Y., Wang, Z.Z., Guo, X., Kek, H.Y., Ku, T., Goh, S.H., Leung, C.F., Tan, E., Zhang, Y., 2024.
850 Three-dimensional reconstruction of subsurface stratigraphy using machine learning with
851 neighborhood aggregation. Eng. Geol. 337, 107588.
852 https://doi.org/10.1016/j.enggeo.2024.107588
853 Jiang, Q.-H., Zhang, J.-Z., Zhang, D.-M., Huang, H.-W., 2024a. Simulation of geological uncertainty
854 based on improved three-dimensional coupled Markov chain model. Eng. Geol. 340, 107647.
855 https://doi.org/10.1016/j.enggeo.2024.107647
856 Jiang, Q.-H., Zhang, J.-Z., Zhang, D.-M., Huang, H.-W., Shi, J.-K., Li, Z.-L., 2024b. Influence of
857 geological uncertainty on longitudinal deformation of tunnel based on improved coupled
858 Markov chain. Eng. Geol. 337, 107564. https://doi.org/10.1016/j.enggeo.2024.107564
859 Liu, H., Luo, Q., El Naggar, M.H., Zhang, L., Wang, T., 2023. Centrifuge Modeling of Stability of
860 Embankment on Soft Soil Improved by Rigid Columns. J. Geotech. Geoenvironmental Eng.
861 149, 04023069. https://doi.org/10.1061/JGGEFK.GTENG-11314
862 Lundberg, S.M., Lee, S.-I., 2017. A unified approach to interpreting model predictions, in: Proceedings
863 of the 31st International Conference on Neural Information Processing Systems, NIPS'17.
864 Curran Associates Inc., Red Hook, NY, USA, pp. 4768–4777.
865 Lyu, B., Hu, Y., Wang, Y., 2023. Data-Driven Development of Three-Dimensional Subsurface Models
866 from Sparse Measurements Using Bayesian Compressive Sampling: A Benchmarking Study.
867 ASCE-ASME J. Risk Uncertain. Eng. Syst. Part Civ. Eng. 9, 04023010.
868 https://doi.org/10.1061/AJRUA6.RUENG-935
869 Lyu, B., Wang, Y., Shi, C., 2024. Multi-scale generative adversarial networks (GAN) for generation of

three-dimensional subsurface geological models from limited boreholes and prior geological knowledge. Comput. Geotech. 170, 106336. https://doi.org/10.1016/j.compgeo.2024.106336
Müller, S., Schüler, L., Zech, A., Heße, F., 2022. GSTools v1.3: a toolbox for geostatistical modelling in Python. Geosci. Model Dev. 15, 3161–3182. https://doi.org/10.5194/gmd-15-3161-2022
Nag, P., Sun, Y., Reich, B.J., 2023. Spatio-temporal DeepKriging for interpolation and probabilistic forecasting. Spat. Stat. 57, 100773. https://doi.org/10.1016/j.spasta.2023.100773
NZGD, 2023. New Zealand Geotechnical Database (NZGD). Available at https://www.nzgd.org.nz.
O'Neill, M.W., 2014. National Geotechnical Experimentation Site: University of Houston. Natl. Geotech. Exp. Sites 72–101. https://doi.org/10.1061/9780784404843.ch04
Pedregosa, F., Varoquaux, G., Gramfort, A., Michel, V., Thirion, B., Grisel, O., Blondel, M., Müller, A., Nothman, J., Louppe, G., Prettenhofer, P., Weiss, R., Dubourg, V., Vanderplas, J., Passos, A., Cournapeau, D., Brucher, M., Perrot, M., Duchesnay, É., 2018. Scikit-learn: Machine Learning in Python. https://doi.org/10.48550/arXiv.1201.0490
Phoon, K.-K., Cao, Z.-J., Ji, J., Leung, Y.F., Najjar, S., Shuku, T., Tang, C., Yin, Z.-Y., Ikumasa, Y., Ching, J., 2022. Geotechnical uncertainty, modeling, and decision making. Soils Found. 62, 101189. https://doi.org/10.1016/j.sandf.2022.101189
Phoon, K.-K., Quek, S.-T., An, P., 2003. Identification of Statistically Homogeneous Soil Layers Using Modified Bartlett Statistics. J. Geotech. Geoenvironmental Eng. 129, 649–659. https://doi.org/10.1061/(ASCE)1090-0241(2003)129:7(649)
Qi, X., Wang, H., Chu, J., Chiam, K., 2022. Effect of autocorrelation function model on spatial prediction of geological interfaces. Can. Geotech. J. 59, 583–600. https://doi.org/10.1139/cgj-2020-0644
Qiu, Y., Zhang, N., Yin, Z., Wang, Y., Xu, C., Zhang, P., 2024. Novel multi-spatial receptive field (MSRF) XGBoost method for predicting geological cross-section based on sparse borehole data. Eng. Geol. 338, 107604. https://doi.org/10.1016/j.enggeo.2024.107604
Robertson, P.K., 1990. Soil classification using the cone penetration test. Can. Geotech. J. 27, 151–158. https://doi.org/10.1139/t90-014
Robertson, P.K., Wride, C. (Fear), 1998. Evaluating cyclic liquefaction potential using the cone penetration test. Can. Geotech. J. 35, 442–459. https://doi.org/10.1139/t98-017
Shi, C., Wang, Y., 2023. Data-driven spatio-temporal analysis of consolidation for rapid reclamation. Géotechnique 1–21. https://doi.org/10.1680/jgeot.22.00016
Shi, C., Wang, Y., 2022. Data-driven construction of Three-dimensional subsurface geological models from limited Site-specific boreholes and prior geological knowledge for underground digital twin. Tunn. Undergr. Space Technol. 126, 104493. https://doi.org/10.1016/j.tust.2022.104493
Shi, C., Wang, Y., 2021. Non-parametric machine learning methods for interpolation of spatially varying non-stationary and non-Gaussian geotechnical properties. Geosci. Front. 12, 339–350. https://doi.org/10.1016/j.gsf.2020.01.011
Shi, C., Wang, Y., Kamchoom, V., 2023. Data-driven multi-stage sampling strategy for a three-dimensional geological domain using weighted centroidal voronoi tessellation and IC-XGBoost3D. Eng. Geol. 325, 107301. https://doi.org/10.1016/j.enggeo.2023.107301
Simm, J., Magrans De Abril, I., Sugiyama, M., 2014. Tree-Based Ensemble Multi-Task Learning Method for Classification and Regression. IEICE Trans. Inf. Syst. E97.D, 1677–1681.

https://doi.org/10.1587/transinf.E97.D.1677
Stuedlein, A.W., 2008. Bearing capacity and displacement of spread footings on aggregate pier reinforced clay (Ph.D.). University of Washington.
Stuedlein, A.W., Kramer, S.L., Arduino, P., Holtz, R.D., 2012a. Geotechnical characterization and random field modeling of desiccated clay. J. Geotech. Geoenvironmental Eng. 138, 1301–1313. https://doi.org/10.1061/(ASCE)GT.1943-5606.0000723
Stuedlein, A.W., Kramer, S.L., Arduino, P., Holtz, R.D., 2012b. Reliability of Spread Footing Performance in Desiccated Clay. J. Geotech. Geoenvironmental Eng. 138, 1314–1325. https://doi.org/10.1061/(ASCE)GT.1943-5606.0000706
Wang, T., Chen, W., Li, T., Connolly, D.P., Luo, Q., Liu, K., Zhang, W., 2023. Surrogate-assisted uncertainty modeling of embankment settlement. Comput. Geotech. 159, 105498. https://doi.org/10.1016/j.compgeo.2023.105498
Wang, Y., Hu, Y., Zhao, T., 2020. Cone penetration test (CPT)-based subsurface soil classification and zonation in two-dimensional vertical cross section using Bayesian compressive sampling. Can. Geotech. J. 57, 947–958. https://doi.org/10.1139/cgj-2019-0131
Wang, Y., Shi, C., 2023. Data-driven analysis of soil consolidation with prefabricated vertical drains considering stratigraphic variation. Comput. Geotech. 161, 105569. https://doi.org/10.1016/j.compgeo.2023.105569
Wang, Z.Z., Hu, Y., Guo, X., He, X., Kek, H.Y., Ku, T., Goh, S.H., Leung, C.F., 2023. Predicting geological interfaces using stacking ensemble learning with multi-scale features. Can. Geotech. J. 60, 1036–1054. https://doi.org/10.1139/cgj-2022-0365
Wu, X., Ma, J., Si, X., Bi, Z., Yang, J., Gao, H., Xie, D., Guo, Z., Zhang, J., 2023. Sensing prior constraints in deep neural networks for solving exploration geophysical problems. Proc. Natl. Acad. Sci. 120, e2219573120. https://doi.org/10.1073/pnas.2219573120
Xiao, T., Li, D.-Q., Cao, Z.-J., Zhang, L.-M., 2018. CPT-Based Probabilistic Characterization of Three-Dimensional Spatial Variability Using MLE. J. Geotech. Geoenvironmental Eng. 144, 04018023. https://doi.org/10.1061/(ASCE)GT.1943-5606.0001875
Xie, J., Huang, J., Lu, J., Burton, G.J., Zeng, C., Wang, Y., 2022a. Development of two-dimensional ground models by combining geotechnical and geophysical data. Eng. Geol. 300, 106579. https://doi.org/10.1016/j.enggeo.2022.106579
Xie, J., Huang, J., Zeng, C., Huang, S., Burton, G.J., 2022b. A generic framework for geotechnical subsurface modeling with machine learning. J. Rock Mech. Geotech. Eng. 14, 1366–1379. https://doi.org/10.1016/j.jrmge.2022.08.001
Xie, J., Zeng, C., Huang, J., Zhang, Y., Lu, J., 2024. A back analysis scheme for refined soil stratification based on integrating borehole and CPT data. Geosci. Front. 15, 101688. https://doi.org/10.1016/j.gsf.2023.101688
Yan, W., Shen, P., Zhou, W.-H., Ma, G., 2023. A rigorous random field-based framework for 3D stratigraphic uncertainty modelling. Eng. Geol. 323, 107235. https://doi.org/10.1016/j.enggeo.2023.107235
Yang, H.-Q., Chu, J., Qi, X., Wu, S., Chiam, K., 2023a. Stochastic simulation of geological cross-sections from boreholes: A random field approach with Markov Chain Monte Carlo method. Eng. Geol. 327, 107356. https://doi.org/10.1016/j.enggeo.2023.107356

Yang, H.-Q., Chu, J., Qi, X., Wu, S., Chiam, K., 2023b. Bayesian evidential learning of soil-rock interface identification using boreholes. Comput. Geotech. 162, 105638. https://doi.org/10.1016/j.compgeo.2023.105638

Yang, Y., Wang, P., Brandenberg, S.J., 2022. An algorithm for generating spatially correlated random fields using Cholesky decomposition and ordinary kriging. Comput. Geotech. 147, 104783. https://doi.org/10.1016/j.compgeo.2022.104783

Yang, Z., Ching, J., 2021. Simulation of three-dimensional random field conditioning on incomplete site data. Eng. Geol. 281, 105987. https://doi.org/10.1016/j.enggeo.2020.105987

Yang, Z., Li, X., Qi, X., 2022. Efficient simulation of multivariate three-dimensional cross-correlated random fields conditioning on non-lattice measurement data. Comput. Methods Appl. Mech. Eng. 388, 114208. https://doi.org/10.1016/j.cma.2021.114208

Zhang, J.-Z., Phoon, K.K., Zhang, D.-M., Huang, H.-W., Tang, C., 2021. Novel approach to estimate vertical scale of fluctuation based on CPT data using convolutional neural networks. Eng. Geol. 294, 106342. https://doi.org/10.1016/j.enggeo.2021.106342

Zhang, J.-Z., Zhang, D.-M., Huang, H.-W., Phoon, K.K., Tang, C., Li, G., 2022. Hybrid machine learning model with random field and limited CPT data to quantify horizontal scale of fluctuation of soil spatial variability. Acta Geotech. 17, 1129–1145. https://doi.org/10.1007/s11440-021-01360-0

Zhang, P., Yin, Z.-Y., Jin, Y.-F., 2022. Bayesian neural network-based uncertainty modelling: application to soil compressibility and undrained shear strength prediction. Can. Geotech. J. 59, 546–557. https://doi.org/10.1139/cgj-2020-0751

Zhang, S., Tao, Y., Geng, X., 2024. A generic random field approach for stratification uncertainty quantification. Eng. Geol. 343, 107800. https://doi.org/10.1016/j.enggeo.2024.107800

Zhang, W., Zhang, R., Wu, C., Goh, A.T.C., Lacasse, S., Liu, Z., Liu, H., 2020. State-of-the-art review of soft computing applications in underground excavations. Geosci. Front. 11, 1095–1106. https://doi.org/10.1016/j.gsf.2019.12.003

Zhao, C., Gong, W., Juang, C.H., Tang, H., Hu, X., Wang, L., 2023. Optimization of site exploration program based on coupled characterization of stratigraphic and geo-properties uncertainties. Eng. Geol. 317, 107081. https://doi.org/10.1016/j.enggeo.2023.107081

Zhao, T., Wang, Y., Lu, S.-F., Xu, L., 2023. Fast stratification of geological cross-section from CPT results with missing data using multitask and modified Bayesian compressive sensing. Can. Geotech. J. 60, 1812–1834. https://doi.org/10.1139/cgj-2022-0131

Zhao, T., Xu, L., Wang, Y., 2020. Fast non-parametric simulation of 2D multi-layer cone penetration test (CPT) data without pre-stratification using Markov Chain Monte Carlo simulation. Eng. Geol. 273, 105670. https://doi.org/10.1016/j.enggeo.2020.105670

Zou, H., Liu, S., Cai, G., Bheemasetti, T.V., Puppala, A.J., 2017. Mapping probability of liquefaction using geostatistics and first order reliability method based on CPTU measurements. Eng. Geol. 218, 197–212. https://doi.org/10.1016/j.enggeo.2017.01.021